

ALMA MATER STUDIORUM · UNIVERSITY OF BOLOGNA

School of Science
Department of Physics and Astronomy
Master Degree in Physics

Implementation and exploitation of new bolometer electronics at ASDEX Upgrade

Supervisor:
Prof. Alessandro Gabrielli

Submitted by:
Alessandro Mancini

Co-supervisor:
Dr. Matthias Bernert

Academic Year 2023/2024

Ai miei genitori Vilma e Alberto...

Abstract

Foil bolometry is a diagnostic technique used in many nuclear fusion machines, like tokamaks and stellarators, to measure the electromagnetic power radiated by thermonuclear plasmas, integrated from near infrared to soft X-rays. ASDEX Upgrade (AUG) is a mid-size tokamak owned by Max Planck Institute for Plasma Physics (IPP), in Munich, which is exploited to conduct highly relevant research in the field of nuclear fusion for energy production. AUG makes use of foil bolometry. A new electronic system has been recently developed by the electronics department of IPP, to improve the time resolution and signal to noise ratio (SNR) of foil bolometers. The aim of this thesis is to characterize the new electronic system and implement a data acquisition and data processing algorithm on an FPGA with the LabVIEW software. The final goal is to implement a new system that performs real-time measurement of the plasma-radiated electromagnetic powers on foil bolometers. The new system is meant to complement an existing one which is already in operation at AUG. The new electronic system has been tested in the laboratory with artificial light sources and has been used in the latest AUG experimental campaign, from October 2024 to January 2025. The new system has been compared to the existing one, to determine whether a signal improvement was achieved.

Contents

1	Introduction to nuclear fusion	3
1.1	Magnetic confinement and tokamak	7
1.2	The tokamak ASDEX Upgrade	11
1.3	Electromagnetic radiation in tokamaks	13
2	Bolometry at ASDEX Upgrade	16
2.1	The bolometer equation	20
3	Foil bolometry electronics	22
3.1	Present foil bolometry electronics	23
3.2	New foil bolometry electronics	25
3.2.1	New bolometer cards	26
3.2.2	National Instrument (NI) modules	27
3.2.3	The Lock-In Amplifier (LIA) technique	28
3.2.4	Low pass filter responses	30
3.2.5	LIA and power reconstruction on RIO FPGA	32
3.2.6	Double frequency Lock-In Amplifier	34
3.2.7	Resource and performance limits	35
3.3	Calibration of foil bolometers	36
4	New bolometry electronics tests	38
4.1	Tests in the laboratory	38
4.2	Tests in the latest AUG campaign	42
5	Summary and outlook	50

Introduction

This thesis focuses on the measurement of electromagnetic radiation produced by a fusion plasma at the tokamak ASDEX Upgrade (AUG), owned by the Max Planck Institute for Plasma Physics (IPP) in Garching (Munich), Germany.

The electromagnetic radiation discussed in this work includes the full spectrum which ranges from Near Infrared (NIR) to soft X-rays, therefore comprising also visible and ultraviolet light. Radiation is of fundamental importance in all nuclear fusion devices since it is produced by various processes during the fusion reactor's operation. Radiation plays an important role in the reactor's power balance since it is an energy loss mechanism, therefore contributing to the Lawson criterion. In addition, radiation plays a crucial role for the power handling on future reactors. The biggest part of the exhaust power has to be radiated in order to protect the wall materials. Therefore, a good measurements of the radiation distribution is essential.

In fusion devices this task is performed by bolometers: diagnostic instruments placed inside the reactor. Bolometers can measure the wavelength integrated absorbed radiation, as power flux (W/m^2) along the path of lines of sight, but do not provide any spectral information.

AUG features two bolometry systems: diode bolometers and foil bolometers. The former are arrays of silicon diodes whose photocurrent is measured and depends on the incident light. Foil bolometers instead are made of small thin metallic foils, thermally connected to resistors, which heat up upon radiation absorption. The resistance change can be measured and correlated to the incident radiative power.

Diode bolometers provide a high time resolution, in the range of some μs , being capable of resolving fast events like ELMs (Edge Localized Modes) and plasma disruptions. However their sensitivity to the electromagnetic spectrum is not linear and they cannot be used for measurement of the total power radiated by the plasma.

Foil bolometers, on the contrary, provide an accurate measurement of the total radiative power but have a lower time resolution, limited to some tens of ms at AUG.

Therefore it is of particular interest being able to increment the time resolution of foil bolometers, which would provide an accurate radiation measurement of fast events during ASDEX Upgrade's operation.

For this purpose a new electronic system has been designed by the electronics department

at IPP. The scope of this thesis is to characterize and test the new electronic system and implement a new data acquisition algorithm on an FPGA with the software LabVIEW. The new electronics have been tested both in the laboratory and in the latest AUG experimental campaign and compared to the existing bolometry electronics to evaluate if the new system brings an improvement in time resolution and signal quality.

The first chapter of this thesis gives an introduction to nuclear fusion, to the tokamak concept and to electromagnetic radiation in tokamaks. The second chapter gives an overview on foil bolometry. The third chapter explains the details of the existing and the new bolometer electronic system at AUG and the new data acquisition algorithm implemented on the FPGA with LabVIEW. The fourth chapter shows the main results obtained with the new system both in the laboratory and in the latest ASDEX Upgrade's experimental campaign, which started in October 2024. Finally chapter five summarizes the main results and suggestions for further developments of this work.

Chapter 1

Introduction to nuclear fusion

Nuclear fusion is a promising candidate energy source to power human activities in the long-term future. It is suitable to be part of the sustainable energy mix. Nuclear fusion does not produce polluting greenhouse gases and the problem of radioactive waste is less critical than in nuclear fission which, however, is becoming more and more manageable. Nuclear fusion has a very high energy yield per unit mass of fuel, higher than nuclear fission and by many orders of magnitude higher than hydrocarbon combustion.

These are the main reasons why there is a great interest, all over the world, in the development of this technology which, however, has a high number of challenges to be solved to become commercially available and economically attractive for countries. Nuclear fusion is in fact not close to becoming a viable energy source in the near future, owing to many challenges, from the physics point of view to the engineering one, as will be discussed in the following. There are many research institutes all over the world and there is an increasing interest by governments and private sector investments, now more than ever. In this picture it is foreseen that the first working fusion reactor prototypes will come in the 2030s and commercial nuclear fusion as a viable energy source will begin probably around 2050/2060.

Nuclear fusion is a type of nuclear reaction for which two light atomic nuclei fuse together producing heavier nuclei. Nuclear fusion reactions are responsible for the power and the production of new elements in the stars, including the sun.

According to Einstein's special theory of relativity, there is a mass difference between the reagent and product nuclei called Q :

$$Q = (M_{reag} - M_{prod}) c^2 \quad (1.1)$$

Q is the energy gained in the reaction, in form of kinetic energy of the product nuclei. If Q is positive the reaction produces net energy.

Nuclear fusion reactions have a threshold: the reagent nuclei need to overcome the

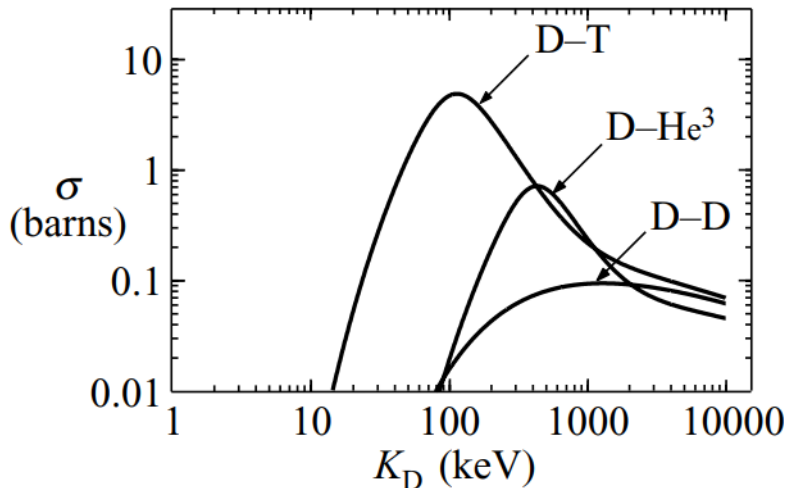
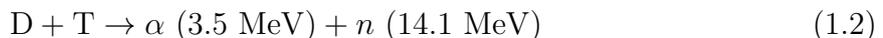


Figure 1.1: [6] cross sections of the most promising nuclear fusion reactions as function of the kinetic energy of the reagents. The D-T (Deuterium - Tritium) is the one with highest cross section at lowest kinetic energy, as compared to the others.

Coulomb electrostatic barrier in order to fuse, which means they need a certain kinetic energy when colliding with each other. Therefore, the probability of fusion occurring depends on the temperature of the reagents.

In nuclear physics the quantity which expresses this probability is the cross section, measured as an area (1 barn = 10^{-24} cm²). Fig. 1.1 shows the cross sections of some candidate fusion reactions to be used in a potential reactor for energy production: Deuterium - Tritium (D-T), Deuterium - Helium 3 (D-³He), Deuterium - Deuterium (D-D). The D-T has the highest cross section at the lowest temperature, therefore, it has the *easiest* conditions to be achieved and has been selected by many scientific programs:



The D-T reaction uses deuterium and tritium: two isotopes of hydrogen, tritium being radioactive with half life of 12.33 years. The reaction has a Q value of 17.6 MeV and produces an α particle (⁴He nucleus) with 3.5 MeV kinetic energy and a fast neutron with 14.1 MeV kinetic energy. In a potential fusion power plant the energy of the neutron is collected as heat by a coolant fluid and transported to the utilities or to a turbine to generate electricity.

From the Q factor one can calculate that a 50% - 50% mixture of D-T produces ~ 340 TJ/kg, that can be compared to ~ 80 TJ/kg for uranium fission and ~ 50 MJ/kg for generic hydrocarbon combustion. This means that 1 kg of D-T is energy equivalent to 4.25 kg of uranium and to 6800 tons of hydrocarbons.

The nuclei of a mixture of D-T have a certain temperature and velocity distribution $f(v)$, which is usually assumed to be a Maxwell-Boltzmann distribution. In the D-T mixture there is a certain number of nuclear fusion reactions happening per unit time. This is expressed through the quantity Reaction Rate, which has the expression:

$$RR = n_D \cdot n_T \cdot \langle \sigma v \rangle \left[\frac{\#}{m^3 s} \right] \quad (1.3)$$

and expresses the number of fusion reactions per unit volume and unit time, where $n_{D/T}$ ($\frac{\#}{m^3}$) are the densities of Deuterium and Tritium nuclei in the mixture and $\langle \sigma v \rangle$ is the product of cross section and velocity of nuclei averaged with the velocity distribution function $f(v)$.

The fusion power per unit volume can be calculated multiplying RR by the energy produced per fusion reaction:

$$P_{fus} = Q \cdot RR \left[\frac{W}{m^3} \right]$$

This implies that to improve the fusion performance a reactor needs high densities and temperature (i.e. nuclei velocities). The optimal temperature at which current D-T reactors aim is around 10 keV (~ 116 million $^{\circ}C$). At this temperature the fuel mixture is fully ionized and is, therefore, in form of plasma.

Plasma is a state of matter composed of free ions and electrons and characterized by quasi-neutrality, meaning there is no net charge. Plasma needs to be confined inside the fusion reactor in order to achieve fusion power and to avoid that it touches the walls. There are no materials on Earth that would withstand the high plasma temperatures required for an efficient fusion reaction for long time.

To confine a plasma there exist currently two approaches:

- magnetic confinement: intense magnetic fields are used to control the plasma particles' trajectories and confine them;
- inertial confinement (not discussed in this thesis): typically intense lasers are used to isotropically compress D-T cryogenic pellets and achieve the desired fusion condition. This approach is investigated for example at the NIF and OMEGA laboratories in the United States [13].

The 2nd approach became well known in the end 2022 when NIF was able to obtain a net fusion energy production, although not fully oriented at reactor studies.

In the magnetic confinement approach the D-T gaseous mixture is heated to fusion temperatures, becoming plasma. The plasma, being ionized and conductive, can sustain

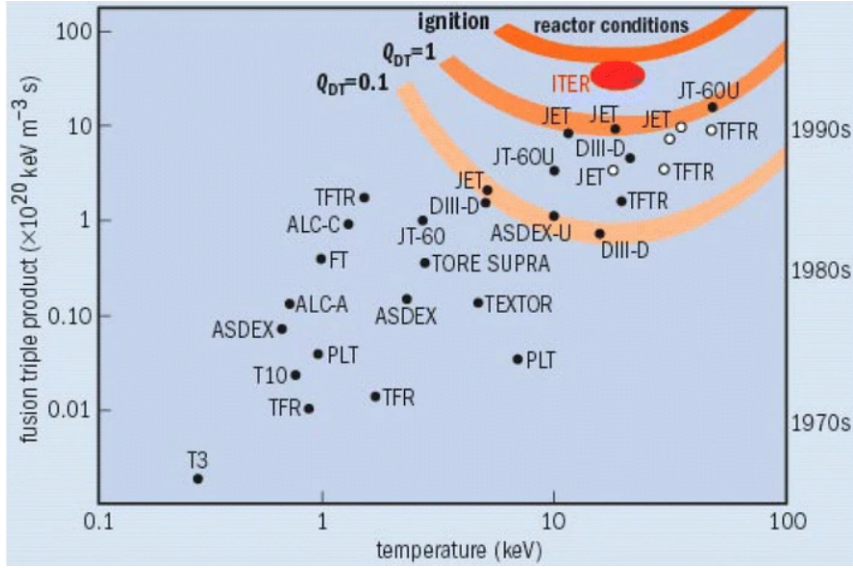


Figure 1.2: [10] triple product $n \cdot T \cdot \tau_E$ for various magnetic confinement reactors. ITER will be the first ever built tokamak to produce net energy (break-even condition).

currents is bound to the magnetic field. Many different magnetic confinement designs exist, the main ones being the tokamak and the stellarator.

Every nuclear fusion device, being it inertial or magnetic confinement, has a performance which can be characterized by the Lawson criterion, which poses a lower threshold on the triple product:

$$n \cdot T \cdot \tau_E \geq 3 \cdot 10^{21} \text{ keV} \cdot \text{s/m}^3 \quad (1.4)$$

This figure of merit quantifies how close a fusion device is to ignition. This is the ultimate goal condition for a reactor. In an ignited plasma the fusion power is sufficient to keep the plasma hot enough to sustain the fusion reaction and compensate the various energy losses mechanisms that cool it down.

In eq. 1.4 n is the already mentioned particle density, T is the temperature and τ_E is the so called confinement time. This is a time constant that indicates how fast a plasma loses its energy due to the various losse mechanisms. So far no magnetic fusion reactor has ever achieved this condition, as shown in Fig. 1.2. No one has even achieved the so called break-even condition, for which the fusion power equates the power required to heat the plasma. ITER is the biggest tokamak now under construction in Cadarache, France. ITER is still not in the ignition range but is designed to reach the break-even condition for the first time in history with magnetic confinement and produce 500 MW net fusion power.

1.1 Magnetic confinement and tokamak

Magnetic confinement makes use of strong magnetic fields to trap the ions and electrons of a plasma. These particles, being charged, are subject to the Lorentz force and move in spirals around the magnetic field lines (gyromotion).

A fusion plasma is a complex medium which is composed of many charged particles of different species: electrons and various types of ions depending on the fuel used and impurities present. All these particles move in the electromagnetic field with defined trajectories and undergo collisions with each other.

Among the magnetic confinement designs the tokamak is currently one of the most promising. The tokamak is a toroidal shaped machine invented by russian physicists in the 1950s. It makes use of different sets of magnetic coils, shown in Fig. 1.3, to produce a helical magnetic field:

- Toroidal Field Coils wrapped around the toroidal chamber, producing the toroidal magnetic field component \mathbf{B}_T . This field is not uniform and its magnitude decreases with the distance from the torus' vertical axis;
- Central Solenoid located vertically in the center of the torus. It runs a pulsed current which induces a secondary current in the plasma itself, acting as an ohmic transformer. The plasma current I_P produces the poloidal component of the magnetic field \mathbf{B}_P ;
- Vertical Field Coils which produce vertical components of the magnetic field, important for plasma control and shaping.

The magnetic field lines resulting from these coils are helical and wrap around the plasma. This is needed to ensure plasma confinement [15].

In a tokamak the magnetic field lines lie on some toroidal surfaces called magnetic flux surfaces. Fig. 1.6 shows a poloidal cross section of the ASDEX Upgrade tokamak where the red curves are the nested magnetic flux surfaces. Since a tokamak needs a plasma current and a central solenoid, it cannot operate in steady state, but is instead a pulsed device. The duration of a pulse, or *shot*, is physically determined by how long the central solenoid can sustain a ramped current. When the current ramp stops the plasma is stopped and a new cycle has to be started again. Typical tokamak pulses currently range from a few seconds to a few minutes.

There exist magnetic confinement reactor designs other than the tokamak which produce a helical magnetic field without the presence of a plasma current. The most notable is the stellarator: a design with specific coils whose geometry ensures the right magnetic field's properties.

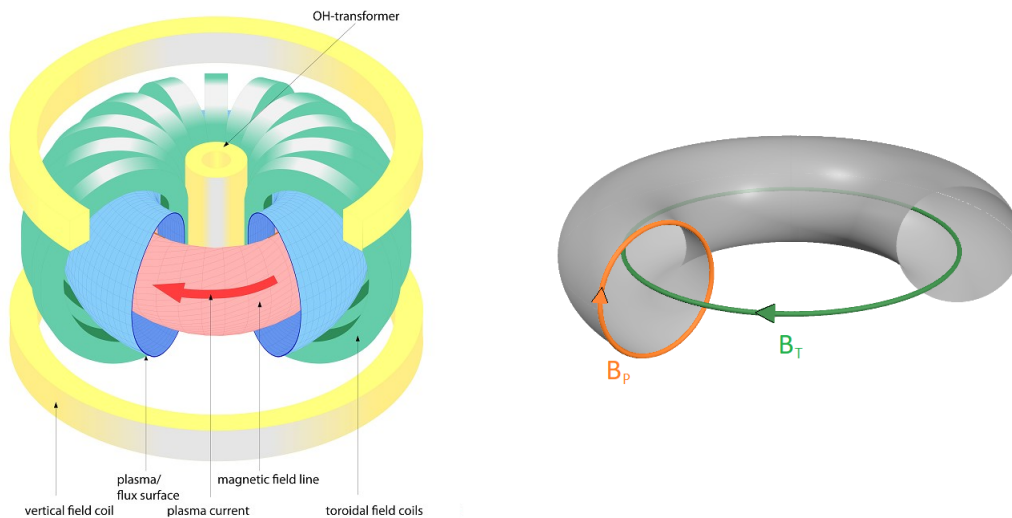


Figure 1.3: (source IPP) simplified scheme of a tokamak with its sets of coils: the toroidal field coils which produce the toroidal field component \mathbf{B}_T ; the central solenoid (OH transformer) that induces the plasma current I_p and the poloidal field component \mathbf{B}_p ; the vertical field coils that produce the vertical component. The resulting magnetic field lines are helical and lie on the flux surfaces.

The inside of a tokamak is evacuated in order to remove atmospheric gas, therefore it's called vacuum vessel. During operation the vacuum vessel is filled with the fuel mixture at very low pressure.

The plasma is initiated by the central solenoid and has to be heated to fusion temperatures. There are currently three techniques for plasma heating:

- ohmic heating: the plasma current I_p itself is able to heat the plasma, which possesses a finite resistance R_p , like any other conductor. The heating power is $R_p \cdot I_p^2$. This method can't heat the plasma indefinitely because the plasma resistance decreases with the temperature [15];
- radio frequency (RF) heating: radio and microwaves can be used to heat ions or electrons. Depending on which species is heated there are two systems: Electron Cyclotron Resonance Heating (ECRH) and Ion Cyclotron Resonance Heating (ICRH). These two systems inject electromagnetic waves with frequency in the range of the particles' gyromotion frequency. This transfers kinetic energy to the particles;
- neutral beam injection (NBI): a beam of high energy neutral particles is injected and collides with the plasma particles in the confined region. This increases temperature, drives plasma current and provides angular momentum.

In order to remove heat and particles that escaped the magnetically confined plasma some tokamaks possess a magnetic configuration called divertor. This configuration separates the plasma into two regions: the confined plasma with nested, closed flux surfaces and the scrape off layer (SOL), where flux surfaces reach the walls. These two zones are divided by a separatrix, as shown in Fig. 1.6 for the tokamak ASDEX Upgrade. Outside of the separatrix the magnetic surfaces are not closed and intersect the divertor target plates. These are designed to withstand high particle and heat fluxes and act as the main region for plasma wall interaction. The particles which end up in the region outside the separatrix follow the magnetic field lines and hit the divertor target plates. The separatrix is, therefore, the last closed flux surface and has an X-point, or null point, where the poloidal component of the magnetic field is null.

The divertor target and tokamak's walls are critical elements because they are the ones which come in contact with the plasma and are called plasma facing components. Therefore, they are made of high temperature tolerant materials, like carbon, molybdenum or tungsten. A critical aspect of these components is that they are eroded by the plasma and pollute it with their elements, which are impurities. This degrades the performance, especially if impurities are transported to the plasma core.

The divertor target is a particular concern for future big tokamaks like ITER where the heat and particle fluxes become enormous.

A tokamak's plasma has different characteristics depending on the region considered. The plasma core is the central part of the confined zone, which has the highest densities, temperature and (in future reactors) fusion reaction rate. Moving away from the core the temperature and densities decrease and the last part of the confined zone, or plasma edge, is reached. The edge has strong gradient on plasma density, temperature and pressure. The region outside of the separatrix is the scrape-off layer, characterized by low plasma temperature and density and high heat fluxes towards the targets.

An important characteristic of tokamaks is the ability to enter the so called high-confinement mode, or H-mode, opposed to the low-confinement, or L-mode. The H-mode is entered at increased heating power. This mode presents an improved confinement, in particular a higher τ_E .

The H-mode is characterized by the formation of a pedestal. This is an increase in the plasma profiles, like temperature and density, which have a steep gradient at the edge, as shown in Fig. 1.4. This increase at the edge leads to higher values in the core. The H-mode is also characterized by the presence of an instability called Edge Localized Mode or ELM. These are edge instabilities that periodically expel bursts of particles and heat onto the plasma facing components [9]. ELMs must be avoided in bigger tokamaks like ITER, as they would lead to unacceptable high heat loads and erosion.

The tokamak has indeed some critical aspects that need to be solved or mitigated in

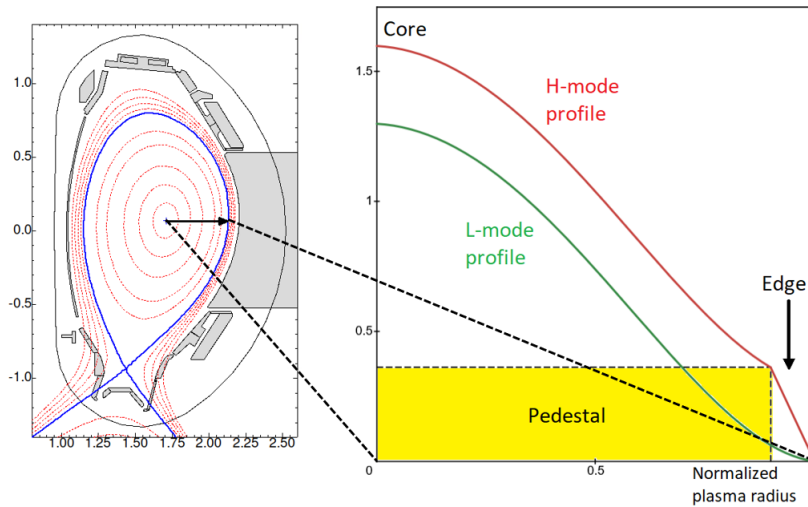


Figure 1.4: pedestal structure. A typical H-mode plasma profile (red), like density or temperature, undergoes a steep gradient at the edge, resulting in higher value in the core. The x-axis is the normalized radius.

order to make it a possible fusion reactor suitable for energy production:

- it is not a steady state machine due to the central solenoid;
- big heat and particle fluxes develop on the plasma facing components;
- it has many plasma instabilities including ELMs and plasma disruptions.

A plasma disruption is a sudden loss of plasma current that can be caused by many factors like impurities or other plasma instabilities. A plasma disruption in a big tokamak is very undesirable because it produces magnetic forces on the reactor's structure that can seriously damage it.

However, the tokamak is a very simple design compared to other concepts like the stellarator. Additionally tokamaks have showed so far the best performance in terms of triple product and energy confinement.

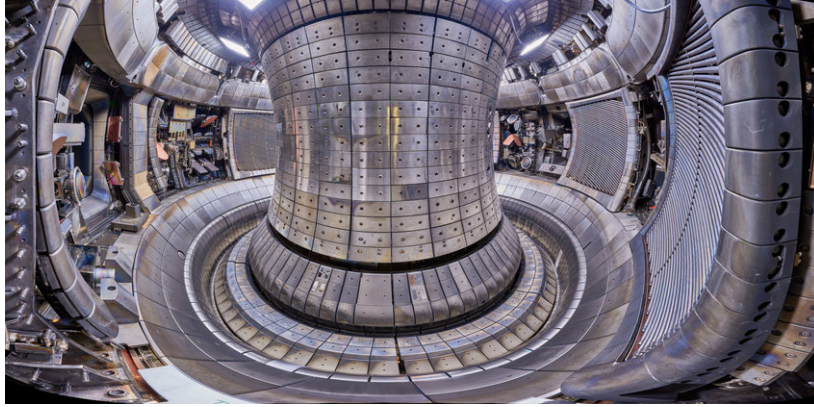


Figure 1.5: (source IPP) view of the tokamak ASDEX Upgrade’s interior. The tokamak’s walls and divertor plates are made of massive tungsten (outer divertor) or tungsten coated tiles to resist the high temperatures and heat fluxes.

1.2 The tokamak ASDEX Upgrade

ASDEX Upgrade (AUG), whose interior is visible in Fig. 1.5, is a medium-sized tokamak owned by the German Max Planck Institute for Plasma Physics (IPP) and located in Garching, Munich.

It started operation in 1991, succeeding its predecessor ASDEX, which operated from 1980 to 1990 and in which the H-mode was first discovered [17]. The name ASDEX is an acronym for Axially Symmetric Divertor EXperiment. AUG in fact allows divertor configurations, as shown in Fig. 1.6, where the magnetic surfaces and separatrix are highlighted. The divertor can be created in the upper part of the tokamak, in the so called Upper Single Null configuration, or in the lower part, called Lower Single Null configuration. The tokamak can also sustain them both, in the Double Null configuration.

AUG has a major plasma radius of 1.65 m, minor radius of 0.5 m and plasma volume of 13 m^3 . Its copper toroidal field coils are capable of producing maximum 3.1 T toroidal magnetic field and its central solenoid allows a plasma current of more than 1 MA. The tokamak can run in L-mode and H-mode and has different plasma heating systems: ICRH, ECRH and NBI for a total of 27 MW heating power.

Plasmas in AUG usually run on deuterium, although the tokamak is able to use also hydrogen and helium. No tritium is used because of its radioactivity and because its handling would imply more strict regulations.

A typical plasma discharge lasts for maximum 10 s, during which the plasma core temperature can reach 10 keV and the particle density 10^{20} m^{-3} .

ASDEX Upgrade cannot produce a burning plasma nor net fusion energy. This tokamak is instead designed to address many relevant problems and open questions that need to

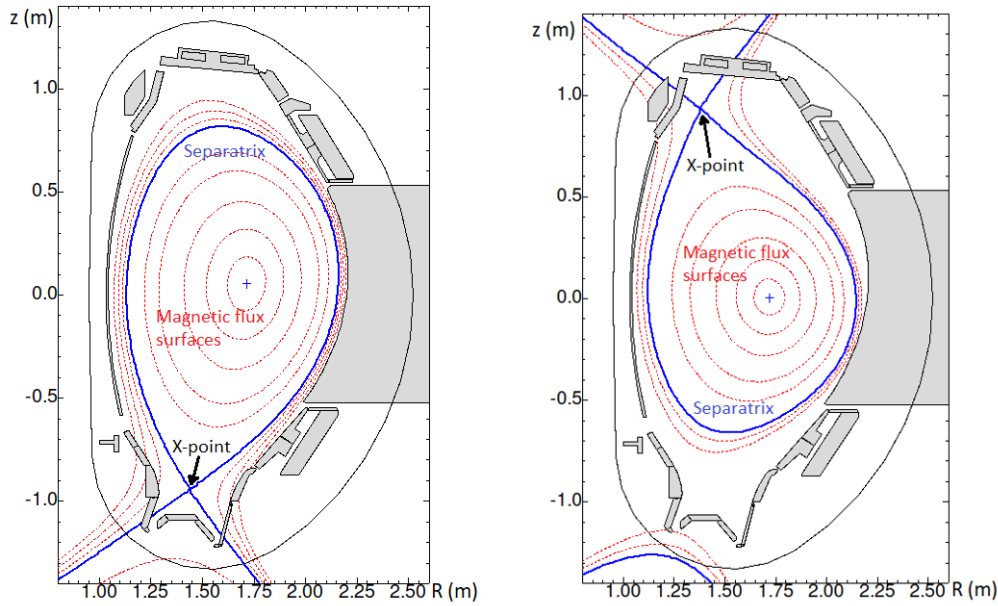


Figure 1.6: (source IPP) poloidal cross section of AUG with magnetic flux surfaces (red), separatrix (blue) and X-point. In gray are the tokamak's structural components. Lower Single Null and Upper Single Null configurations respectively on left and right.

be solved for future tokamaks like ITER. AUG features in fact a full tungsten wall and divertor plates, like ITER will. Tungsten is a heavy metal, selected due to its low erosion rate and high melting temperature above 3000 °C. However, being a high Z material, tungsten is a very undesired impurity in the plasma since it is not fully ionized even in the plasma core and can dissipate a significant part of the plasma energy through electromagnetic radiation.

AUG possesses a great number of diagnostic systems which can measure several physical quantities of interest, like particle density, magnetic field, radiation, current.

The research conducted with ASDEX Upgrade at Max Planck Institute for Plasma Physics is of great importance for the development of nuclear fusion and addresses several topics including plasma particle and impurity transport, plasma instabilities and turbulence, study of relevant nuclear reactor scenarios, heat exhaust on divertor and wall, wall erosion and damage, numerical methods and plasma simulations.

ASDEX Upgrade underwent a two-years maintenance and construction phase which ended in July 2024 during which new diagnostics and new upper divertor tiles have been installed. The new upper divertor features a new set of coils which will be used to create particular divertor configurations, part of the Advanced Divertor Configuration (ADC) research [2].

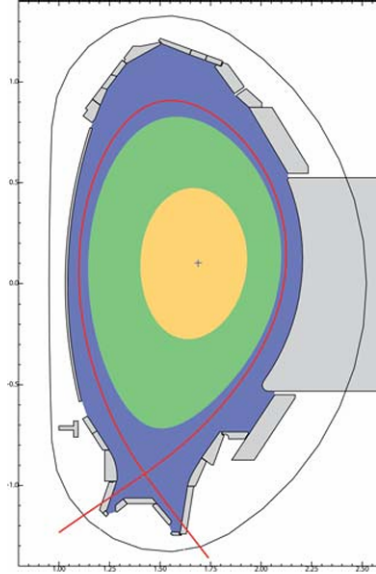


Figure 1.7: [5] AUG's plasma divided into three regions based on the radiation's characteristics: the plasma core (yellow) where bremsstrahlung dominates, the intermediate region (green) and the edge and divertor (blue) where the temperature is lower and line radiation dominates.

1.3 Electromagnetic radiation in tokamaks

A thermonuclear plasma needs to be heated in order to reach the fusion conditions and needs to be maintained at such high temperature. The power balance of a fusion plasma includes different terms: the input power P_{in} (ECRH, ICRH, NBI), the produced fusion power P_{fus} and the losses P_{loss} that cool the plasma down. The losses need to be compensated in order to maintain the plasma hot enough to sustain the fusion reaction. In present magnetic confinement devices the P_{fus} contribution is still not sufficient to compensate the losses, therefore the power balance is:

$$P_{fus} + P_{in} = P_{loss}$$

The ultimate goal for future reactors is to reach ignition: a condition for which the fusion power P_{fus} is at least equal to the losses and there is no more need for input power [6]:

$$P_{fus} = P_{loss} \tag{1.5}$$

In a D-T plasma the term P_{fus} includes only the alpha particles' energy, because neutrons, being electrically neutral, cannot be magnetically confined and cannot transfer their energy to the plasma. From eq. 1.5 the Lawson criterion is derived (eq. 1.4).

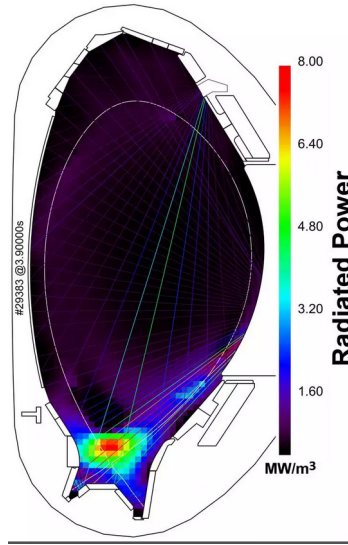


Figure 1.8: [14] tomographic reconstruction from bolometry lines of sight showing the radiation distribution inside ASDEX Upgrade. A strongly radiating region near the X-point can be observed (X-point radiator).

The term P_{loss} includes multiple contributions, the main ones being conduction loss and radiation loss. The conduction loss arises from the collisions between the plasma particles and the plasma facing components (wall, divertor) and is accompanied by a particle loss. The plasma can dissipate energy also through electromagnetic radiation.

There are several phenomena that produce electromagnetic radiation in a tokamak. The plasma can be divided into multiple regions depending on the radiation characteristics, as shown in Fig. 1.7. The plasma core (yellow) is the region with the highest temperature, in the keV range. The dominant radiation source here is bremsstrahlung, produced by collisions between electrons and ions. If there are high Z impurities present, like tungsten, also line radiation plays a role, adding an important contribution to the plasma energy loss. Tungsten is not fully ionized even in the plasma core and can radiate much energy. For this reason the tungsten content in the plasma core has to be limited.

The second intermediate region (green) has lower temperatures and here the contribution of line radiation from lighter impurities becomes more important.

Finally in the edge and divertor region (blue) the temperature is lower (1 - 100 eV). Here line radiation is the dominant source, especially by deuterium, in the infrared, visible and ultraviolet portions of the spectrum.

The divertor plates are subject to the heat and particle flux coming from the scrape-off layer. ELMs produce particularly high heat bursts that put the divertor tiles to the test. This is especially a concern for big tokamaks like ITER.

A possibility to attenuate the heat flux is exploiting electromagnetic radiation, through impurity seeding. This is a technique which foresees the injection of light elements (impurities), like nitrogen or argon, inside the plasma. These impurities become partially ionized and produce intense line radiation, especially in the scrape-off layer and divertor regions. Radiation helps distributing the heat flux over a larger area and attenuates the load on the divertor plates, creating a local cooling.

Electromagnetic radiation is, therefore, an important factor to be measured in a tokamak. It is both an energy loss mechanism that limits the fusion performance and a tool that can be used to reduce the thermal stress on the plasma facing components.

Part of the research conducted at ASDEX Upgrade is aimed at studying the XPR regime and how the radiation production is distributed inside a tokamak. The diagnostic instruments designed for measuring radiation are bolometers. They can measure the radiative power produced by the plasma integrated along lines of sight.

With bolometers it is possible to perform tomographic reconstructions and obtain the radiation distribution inside the fusion reactor, as W/m^3 . Fig. 1.8 shows an example of tomographic reconstruction where it's possible to visualize a strongly radiating toroidal ring close to the X-point. This regime, achieved at high impurity seeding level, is called X-Point Radiator (XPR) [4]. The position of the XPR can be actively controlled using bolometry lines of sight.

Chapter 2

Bolometry at ASDEX Upgrade

This chapter describes the bolometry technique used to measure the electromagnetic power radiated by a fusion plasma, with emphasis on foil bolometers at ASDEX Upgrade. The physical principle of foil bolometers, along with the formulas used for power calculation, are explained.

Bolometers are detectors used in many areas of science to measure the radiant power emitted by a hot body. Ideally bolometers are sensitive to a broad electromagnetic spectrum, ranging from microwaves to soft X-rays. Bolometers do not give any spectral information: they measure the wavelength integrated absorbed power.

In the context of nuclear fusion, bolometers are the diagnostic system used to measure radiation produced by plasmas. Most existing and future magnetic confinement fusion reactors feature bolometers.

This chapter introduces the bolometry technique, with emphasis on foil bolometry at ASDEX Upgrade.

ASDEX Upgrade (AUG) features two systems of bolometers to measure radiation: AXUV diode bolometers [3] and foil bolometers.

Diode bolometry exploits AXUV16ELG, manufactured by Opto Diode. These are arrays of 16 silicon photodiodes powered by a bias voltage. The incident radiation produces a measurable photocurrent, through electron-hole production in the sensitive volume of the diodes. The photocurrent depends on the intensity of the incident radiation.

AXUV diodes have a time resolution of few μs and are capable of resolving fast events like ELMs and plasma disruptions. Their sensitivity to radiation ranges from near infrared to soft X-rays but it is not linear. In particular it is low in the VUV (Vacuum Ultraviolet) region between 2 eV and 200 eV. Most of the line radiation emitted by hydrogen and deuterium is within this region. Therefore AXUV diodes underestimate the total radiated power by the plasma.

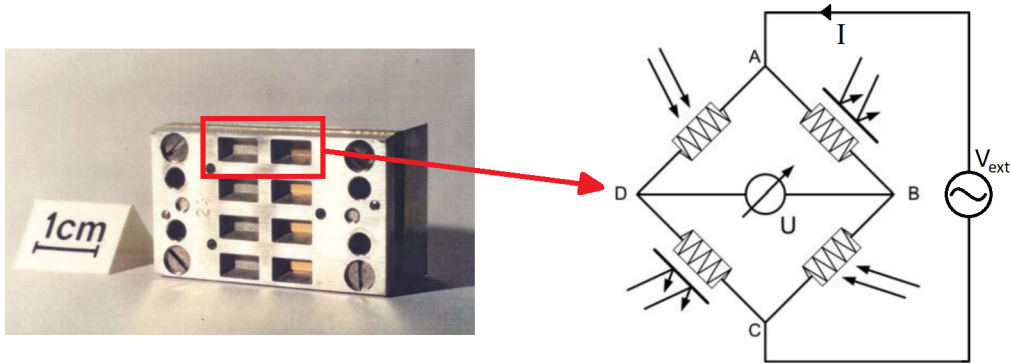


Figure 2.1: (source IPP) left: a foil bolometer head containing four channels. Right: one channel comprises two foils (one masked and one exposed) and four resistors (two per each foil), arranged in a Wheatstone bridge configuration. A voltage excitation V_{ext} is applied to points A, C and the response voltage U at points D, B is measured.

Foil bolometers exploit thin metallic foils thermally connected to resistors. The impinging photons deposit their energy in the foil, whose temperature increases.

At AUG each foil is made of a $5\ \mu\text{m}$ layer of gold deposited on a $4.5\ \mu\text{m}$ layer of silicon nitride electrical insulator [7]. In order to increase the foils absorption in the visible range they are coated with carbon. The foils absorb practically all the photons energy in the sensitive spectrum (near infrared to soft X-ray) without any wavelength dependence in the measurement. This allows foil bolometers to be used to perform total radiated power measurement, unlike diode bolometers.

Each foil is thermally connected to two platinum meander-like resistors, $\sim 1.2\ \text{k}\Omega$ each, shown in Fig. 2.2. One bolometer channel comprises four resistors, i.e. two foils: one is masked, the other is exposed to the plasma. The masked foil is not affected by the incident radiation and allows to compensate the drifts induced by the environmental temperature changes. The four resistors of a channel, two exposed and two masked, are connected in a Wheatstone bridge configuration as shown in Fig. 2.1. The resistivity of the exposed resistors increases when the foil's temperature increases owing to incident radiation. An excitation voltage V_{ext} ($\sim 10\ \text{V}$) is applied to points A, C and the response voltage U ($\sim 10\ \text{mV}$) across points D, B is measured. With this measurement it is possible to accurately evaluate the bridge's mismatch, i.e. the difference between active and passive resistances. The mismatch is correlated to the temperature of the exposed resistors. In a traditional Wheatstone bridge only one resistor is variable and measured. In foil bolometers, instead, the fact that two resistors are measured allows to measure double the signal.

The response voltage U allows to obtain the incident power on the foil through the

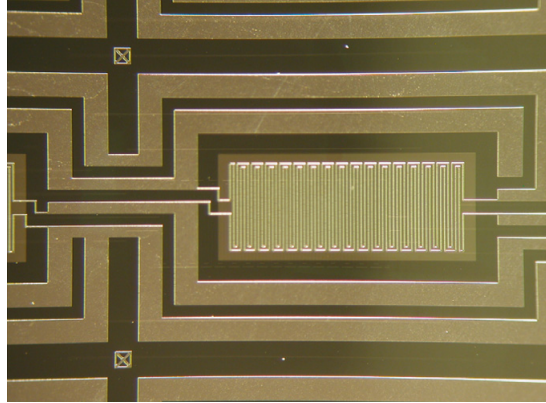


Figure 2.2: [7] close zoom of the two platinum meander resistors placed behind one foil of one bolometer.

bolometer equation [8]:

$$P_{\text{in}}[\text{W}] = C \cdot \left(\frac{U}{\tau} + \frac{dU}{dt} \right) \quad (2.1)$$

where C [J/V], τ [s] are respectively the bolometer's heat capacity and cooling time and depend on the thermal properties of the foils. The cooling time τ is related to the time needed to dissipate the heat from the foil to the bolometer's structure and its value is between 50 - 200 ms. It is not this time constant which physically limits the time resolution of the instrument. What limits it is the time needed by the heat to propagate from the foil to the meander resistors, which is in the order of few μs .

To obtain C , τ there exist different calibration procedures, analysed in chapter 3, sections 3.3.

Since the resistors in each Wheatstone bridge are not perfectly identical practically all bolometers measure some voltage U even without the presence of radiation, which constitutes an offset that has to be taken into account.

A bolometer head, shown in Fig. 2.1, 2.3, includes four bolometer channels and has electrical pins connected to the meander resistors. One or more heads are mounted on a bolometer camera, which has a small pinhole and no optics: the foils are directly exposed to the incident radiation coming from the plasma. Fig. 2.4 shows a scheme of a bolometer camera on the left and on the right a set of three cameras (FVC, FHC, F01) mounted on ASDEX Upgrade with their lines of sight.

The incident power obtained with eq. 2.1 is divided by the bolometer camera's etendue to obtain the power radiated by the plasma per unit surface [W/m^2]. The etendue is a geometrical characteristic of the camera determined by the pinhole and foil areas and the distance between them.

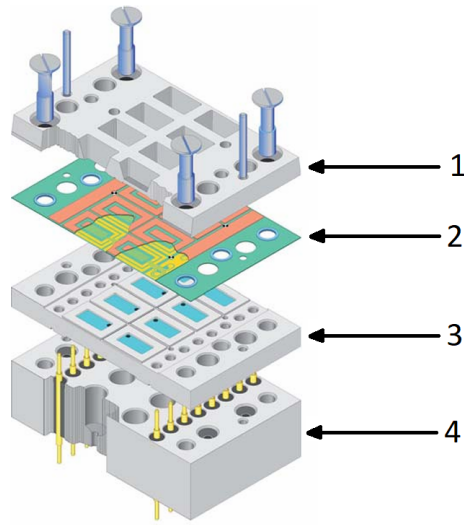


Figure 2.3: [12] scheme with components of a bolometer head. 1. Front plate. 2. Bolometer foils. 3. Back cooling plate. 4. Support plate with electric contacts for the resistors.

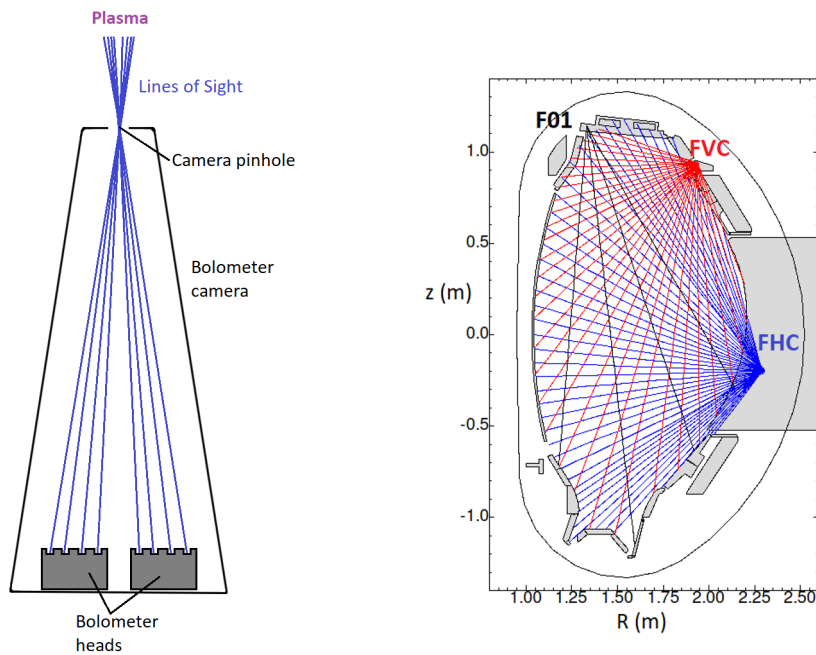


Figure 2.4: (source IPP) left: scheme of a foil bolometer camera with lines of sight (LOS). Right: set of the LOS of three foil bolometer cameras: Foil Horizontal Camera (FHC) with 48 LOS, Foil Vertical Camera (FVC) with 32 LOS, F01 camera with 4 LOS.

2.1 The bolometer equation

The bolometer equation 2.1 comes from a power balance. The energy (heat) absorbed by the foil goes into two contributions: it increments the foil's temperature T and is dissipated to the surroundings with a time constant τ . Therefore it is possible to write an equation as follows:

$$E_{in}[J] = C' \cdot \left(dT + \frac{T}{\tau} \right) \quad (2.2)$$

where T has to be interpreted as the temperature difference between the exposed foil and the environment. It is this temperature difference which dissipates the heat from the exposed foil to the bolometer's structure. The term $C' \cdot dT$ is related to the heating of the foil; the term $C' \cdot T/\tau$ is related to the heat dissipation.

The temperature variation dT is proportional to the resistance variation dR of the exposed resistors, which is in first approximation proportional to U . Eq. 2.2 becomes:

$$E_{in}[J] = C \left(U + \int \frac{U}{\tau} dt \right) \quad (2.3)$$

Eq. 2.1 is found by differentiating eq. 2.3 with respect to time.

The excitation voltage V_{ext} provided to each Wheatstone bridge is a waveform with fixed amplitude. Since a bolometer is a resistor network, the response voltage U is a waveform as V_{ext} . There is, however, a phase shift introduced by the parasitic capacitance and inductance of the long connecting cables. The amplitude of U is modulated by the incident radiation, with eq. 2.1 describing its behavior.

When there is no incident power on the foil ($P_{in} = 0$ W) eq. 2.1 becomes:

$$\frac{dU}{dt} = -\frac{U}{\tau} \quad (2.4)$$

which leads to a simple decreasing exponential solution:

$$U(t) = U_0 e^{-t/\tau} \quad (2.5)$$

If the foil is subject to a constant incident power P eq. 2.1 gives the solution:

$$U(t) = \frac{P}{C} \tau + U_0 e^{-t/\tau} \quad (2.6)$$

Equations 2.5 and 2.6 show that the response voltage's amplitude reacts with an exponential behavior to a steep power transient, as can be seen in Fig. 2.5.

The goal of the foil bolometry data acquisition (DAQ) electronics is to perform amplitude demodulation of U and use the amplitude in eq. 2.1 to obtain the incident power.

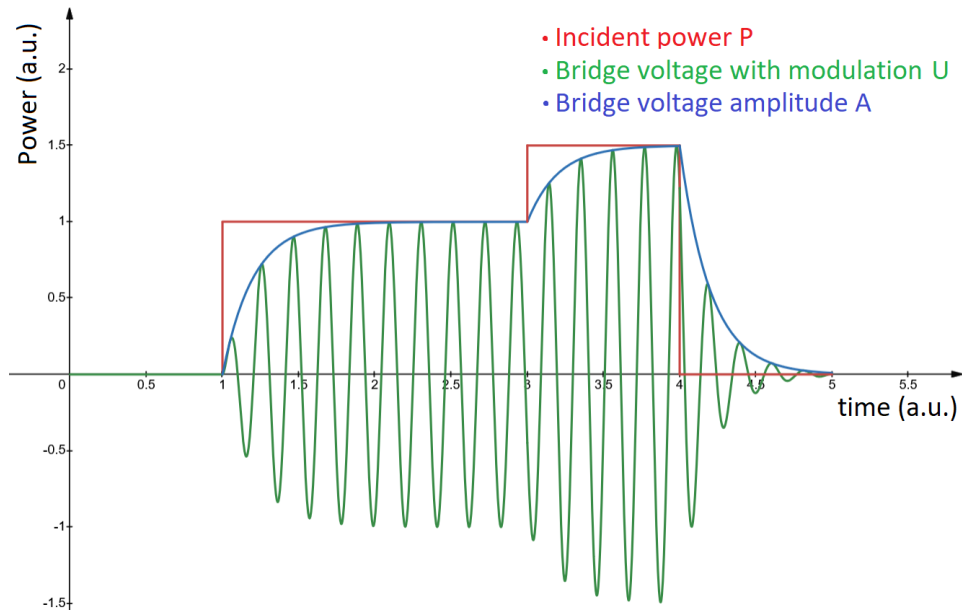


Figure 2.5: the response voltage U (green) is modulated by the incident radiative power (red). The amplitude's behavior (blue) is exponential with time constant τ for a steep power transient.

The DAQ system is responsible for producing the excitation waveform V_{ext} and acquiring the response voltage U for all the bolometer channels. The critical point is that the electronics have to be capable of resolving small signals in a noisy environment. Noise must be suppressed as much as possible since the bolometer equation includes a derivative. This is a particular concern in data acquisition since the derivative amplifies all the noise present in U .

By properly choosing the excitation waveform's shape and frequency it is possible to perform amplitude demodulation techniques to reduce noise.

Chapter 3

Foil bolometry electronics

This chapter describes the foil bolometry electronics currently in operation at ASDEX Upgrade and the new one recently developed and tested in this thesis. The Lock-In Amplifier technique for sinusoidal amplitude demodulation is introduced. The digital Lock-In Amplifier algorithm developed for a National Instrument FPGA with the LabVIEW software is presented.

The electronics analysed in this thesis perform digital data acquisition (DAQ). This means that waveforms and signals are sampled by an Analog to Digital Converter (ADC) and represented as a series of time points (samples) acquired with a certain sampling rate (SR) which defines the time interval between every two time points. The ADC is an electronic component designed to sample a physical quantity, usually a voltage. An ADC is characterized by an operational voltage window $[V_{min}, V_{max}]$ and by a number of bits. These parameters define the voltage resolution of the ADC. As example, the resolution of a $[-10.24 \text{ V}, +10.24 \text{ V}]$ 16 bit ADC is:

$$dV = \frac{20.48 \text{ V}}{2^{16}} = 0.3125 \text{ mV/bit} \quad (3.1)$$

the samples acquired with such an ADC are represented as 16 bit integers with 0 corresponding to -10.24 V and $65535 (2^{16}-1)$ to $+10.24 \text{ V}$.

Every ADC has an intrinsic noise, which is in the range of the last few bits, therefore reducing the actual possible resolution.

In digital DAQ the signals are processed through digital signal processing (DSP) techniques, which allow to perform arithmetic operations between the samples of a signal.

Another important component in digital electronics is the Digital to Analog Converter (DAC). This component performs the opposite task of the ADC, converting digital numbers into voltages. A DAC can be used to create offsets and to produce a certain waveform starting from a series of digital samples.

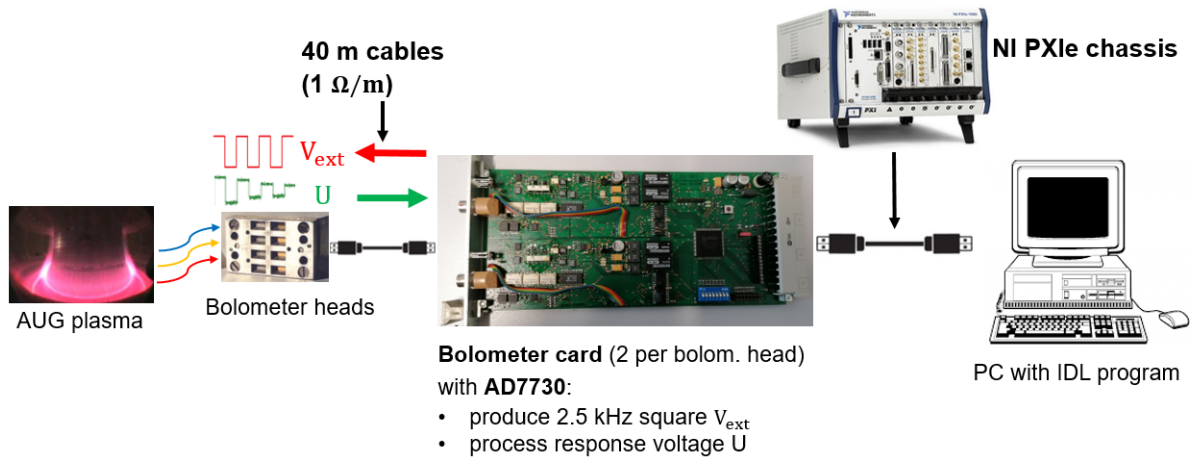


Figure 3.1: DAQ chain of the present foil bolometry electronics. The bolometer heads are connected to bolometer cards which embed AD7730 chips, that produce the 2.5 kHz V_{ext} and process the response voltages U . The signals are post-processed by a PC with IDL program which reconstructs the incident powers on the bolometers.

3.1 Present foil bolometry electronics

The DAQ chain of the present foil bolometry electronics is shown in Fig. 3.1. The bolometer heads, placed inside the tokamak, are connected, through 40 m cables, to bolometer cards designed in-house at AUG. The cards produce the excitation waveforms V_{ext} and process the response voltages U through the AD7730 [1] integrated circuit, manufactured by Analog Devices. This chip is specifically designed as a front-end for Wheatstone bridge and has 24 bit ADC embedded. V_{ext} is a 2.5 kHz, ± 5 V (10 V peak to peak) square wave, generated by the AD7730 by periodically switching 5 V between the sides of the Wheatstone bridge.

After every flank of V_{ext} the AD7730 waits 50 μs to avoid the transient voltage period of U . Then it performs an acquisition of the Wheatstone bridge's response voltage U over few μs . One ADC value for each square wave's stable level is obtained, through internal digital filters included on the AD7730. Therefore, the sampling rate of the signals is 2.5 kHz. Only 16 of the ADC's 24 bits are kept in the bolometer electronics: the last 8 bits are removed as they are below the noise level.

The bolometer cards are interfaced to a National Instrument (NI) chassis embedding a controller with CPU (NI PXI-8108) and FPGA (NI PXI-7813R) that handles the DAQ, stores data and transfers it to the AUG servers for storage.

During an AUG discharge a DAQ run lasts for 16 seconds and collects the bolometer signals processed by the AD7730. The derivatives of the signals (see eq. 2.1) are calculated on the NI PXI FPGA through a Savitzky-Golay filter.

The collected signals are analysed in post processing on a PC through an IDL program

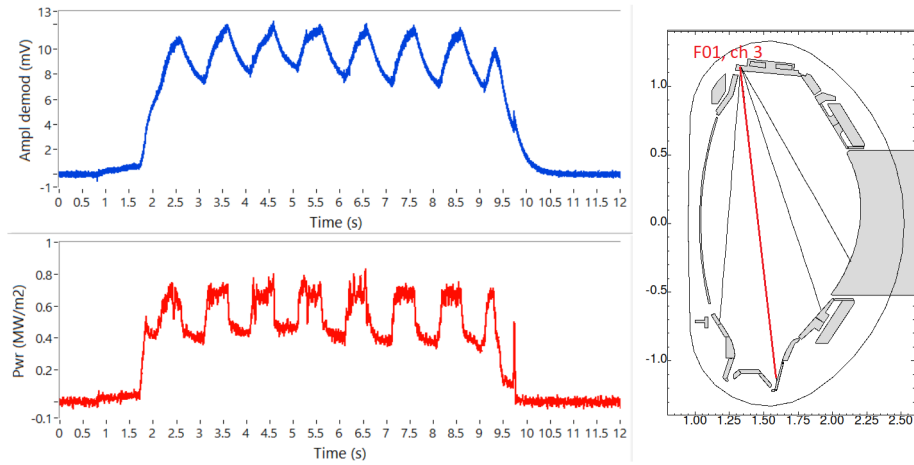


Figure 3.2: (real data) example of bolometer signals of an AUG plasma discharge, camera F01, channel 3. The upper plot is the Wheatstone bridge demodulated voltage U . The lower plot is the reconstructed power $[\text{W}/\text{m}^2]$.

which performs a boxcar average with 31 samples width. This helps decreasing noise but also reduces time resolution. The IDL program obtains the incident power reconstruction, through eq. 2.1 and divides it by the bolometer camera's etendue, to obtain the power per surface unit. Fig. 3.2 shows an example of a 16 s DAQ run for one bolometer channel (FVC camera, ch 9) with the discussed electronics.

With the applied filters the time resolution of the current bolometer electronics is 15 ms (66 Hz). This means that the electronics are able to resolve a signal with maximum frequency of 66 Hz. Signals that are faster than this will be smoothed too much by the filtering, which is required to remove the high level of noise. The latter comes from several systems needed to run the tokamak, like ECRH and power supplies. The critical part of foil bolometry are the 40 m cables that connect the bolometers to the electronics and are responsible for picking up noise.

The bolometer cards have mechanical relays that can switch between *measurement mode* and *calibration mode*. The former is used to drive the Wheatstone bridge and acquire data, during AUG discharges. The latter, discussed in Sec. 3.3, is used to obtain the bolometers' calibration constants C , τ .

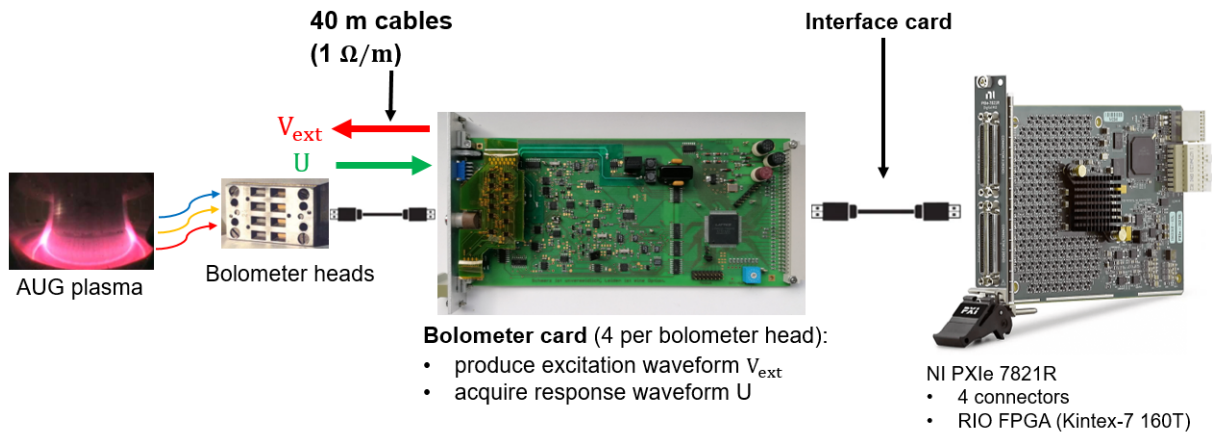


Figure 3.3: DAQ chain of the new bolometer electronic system. The bolometer cards produce the excitation waveform V_{ext} for the bolometers and acquire the response voltages U , which are real-time transmitted to the NI PXIe 7821R module which performs amplitude demodulation.

3.2 New foil bolometry electronics

The new foil bolometry DAQ chain is shown in Fig. 3.3. The new bolometer cards have been recently developed in-house at AUG by the electronics department and have different characteristics and improvements with respect to the previously described cards, the main ones being:

- possibility of inducing any type of excitation waveform V_{ext} , such as square, sinusoidal, sawtooth, triangular;
- possibility of sampling the full waveform period.

By inducing different types of excitation waveform the new cards allow to exploit different amplitude demodulation and noise reduction techniques. The switching transients, which induce noise and are typical of a square waveform, can be avoided if a non-square excitation is used. This thesis studies the use of a sinusoidal excitation.

The possibility to sample the full waveform period allows to record the response voltages U and to better characterize the noise sources. With the present foil bolometry electronics this is not possible: the response voltages are processed by the AD7730 and are not recorded.

The bolometer cards communicate, through an interface card, to a National Instrument (NI) PXIe chassis which embeds CPU (NI PXIe 8861) and FPGA (NI PXIe 7821R, shown in Fig. 3.3). The aim of this thesis is to characterize the new bolometer cards and develop a new amplitude demodulation and power reconstruction algorithm that runs on the NI FPGA, in order to realize a real time DAQ system and explore its performance.

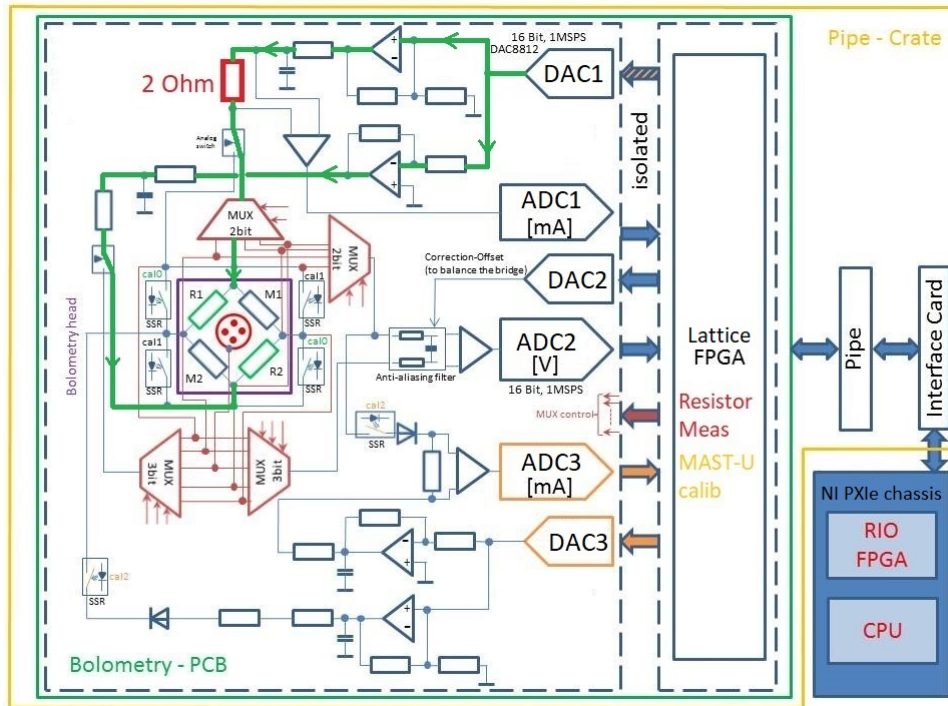


Figure 3.4: new bolometer card’s simplified electrical diagram. Each card has one connector for one bolometer channel (Wheatstone bridge) and features three DACs and three ADCs. The blue rectangle indicates the NI PXIe chassis with RIO FPGA (PXIe 7821R) and CPU. An interface card connects the bolometer card to the NI chassis.

3.2.1 New bolometer cards

Fig. 3.4 shows the main components of the new bolometer cards, developed by the AUG electronics department, which are responsible for producing the excitation waveform for the bolometers and acquiring the response voltages. Each card is connected to a bolometer channel through a 40 meter four pin cable. The purple square in Fig. 3.4 represents the connection to the Wheatstone bridge, where R1/2 are the reference (passive) resistors, M1/2 are the measuring (active) resistors.

Each bolometer card features three 16 bit DACs (DAC8812, by Texas Instruments) with range ± 10 V and three 16 bit ADCs (LTC2328-16, by Linear Technology) with range ± 10.24 V.

A small FPGA manufactured by Lattice Semiconductors handles the internal control of the card and the communication with the external NI PXIe chassis.

DAC1 in Fig. 3.4 produces the excitation waveform for the Wheatstone bridge, which can be, for example, square, sinusoidal, sawtooth or triangular with adjustable frequency. The output of DAC1 is fed to two operational amplifiers which supply the waveform to

the Wheatstone bridge (green paths in Fig. 3.4). V_{ext} can go from -20 V to +20 V. The other DACs are responsible for performing calibration pulses or compensating offsets due to unbalanced bridges.

The ADCs are responsible for the data acquisition and support up to 1 MHz sampling rate. They have 0.3125 mV/bit resolution. ADC1 in Fig. 3.4 measures the total current that crosses the bolometer, by measuring the voltage drop across a 2 Ω shunt resistor (highlighted in red in Fig. 3.4). ADC2 measures the response voltage U of the Wheatstone bridge. ADC3 is used for the calibration. The ADCs include amplification stages of the measured voltages: a first amplification stage of 100 is applied; a second amplification stage, from 2 to 16, can be controlled with the small Lattice FPGA on the card.

Each bolometer card has some solid state relays (SSR), controlled by the Lattice FPGA, which allow to short-circuit some segments and change some connections. The SSRs are used to perform resistance measurements and are exploited in the calibration procedures, as will be discussed in Sec. 3.3.

3.2.2 National Instrument (NI) modules

The bolometer cards communicate with a National Instrument chassis (NI PXIe 1082) through in-house developed interface cards. The NI chassis is equipped with two modules:

- NI PXIe 8861 controller with CPU and Linux Real-Time OS;
- NI PXIe 7821R which embeds a Kintex-7 FPGA, manufactured by Xilinx/AMD. This will be referred to as RIO FPGA (Reconfigurable I/O FPGA), as it is called in the National Instrument ecosystem.

The NI controller runs a LabVIEW interface used for starting and handling the DAQ on the RIO FPGA and storing the signals acquired.

The RIO FPGA is used to process in real time the signals acquired by the bolometer cards (response voltages, currents) and calculate the incident powers on the bolometers. The RIO FPGA can be programmed with the LabVIEW FPGA suite, which allows to create firmware that is uploaded on the RIO FPGA and is deterministic and independent of external conditions. Within this thesis an amplitude demodulation and power reconstruction algorithm, for sinusoidal excitation V_{ext} , has been implemented and tested on the RIO FPGA. The chosen algorithm to perform amplitude demodulation is the Lock-In Amplifier, which is presented in the following section.

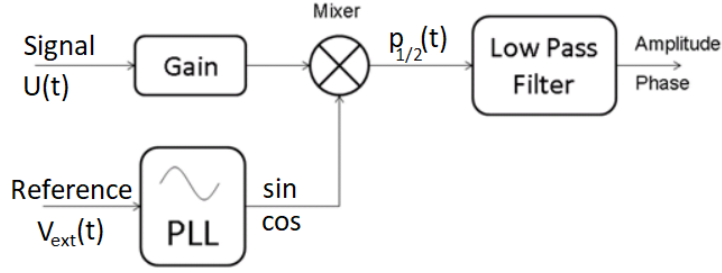


Figure 3.5: Lock-In Amplifier scheme. Its main components are the Phase Locked Loop (PLL), mixer and Low Pass Filter.

3.2.3 The Lock-In Amplifier (LIA) technique

The Lock-In Amplifier (LIA) is a technique which recovers the amplitude and phase of a sinusoidal signal with known frequency from a noisy environment. This is the chosen technique to perform amplitude demodulation of the bolometers response voltages. A sinusoidal excitation waveform V_{ext} with fixed amplitude and frequency f_{ext} is applied to the Wheatstone bridges. The response voltages U are sinusoidal waveforms whose amplitude is modulated by the incident radiation on the bolometer, as explained in Sec. 2. The components of a basic LIA are shown in Fig. 3.5, where the input signal is the response voltage U of one bolometer channel. Figures 3.6, 3.7 show how a LIA works:

- the **Phase Locked Loop (PLL)** generates, starting from a reference waveform (V_{ext}) two clean sine and cosine waveforms that have 90° phase difference and are phase-locked to the input signal;
- the **mixer** multiplies the input signal separately by the sine and cosine, producing two new waveforms p_1, p_2 which have a $2 \cdot f_{\text{ext}}$ frequency component;
- the **Low Pass Filter (LPF)** is used to remove this frequency component from $p_{1/2}$, producing the filtered waveforms $p'_{1/2}$;
- the amplitude and phase of U can be reconstructed with the formulas in Fig. 3.7:

$$A = 2 \cdot \sqrt{(p'_1)^2 + (p'_2)^2} \quad (3.2)$$

$$\phi = \tan^{-1}(p'_2/p'_1) \quad (3.3)$$

The PLL is a feedback component, which takes V_{ext} as input reference and generates a sine and cosine waveforms, which are phase locked to it. This component constantly minimizes the phase difference between the reference and the sine/cosine waveforms. This is needed to accomodate phase changes in U over time.

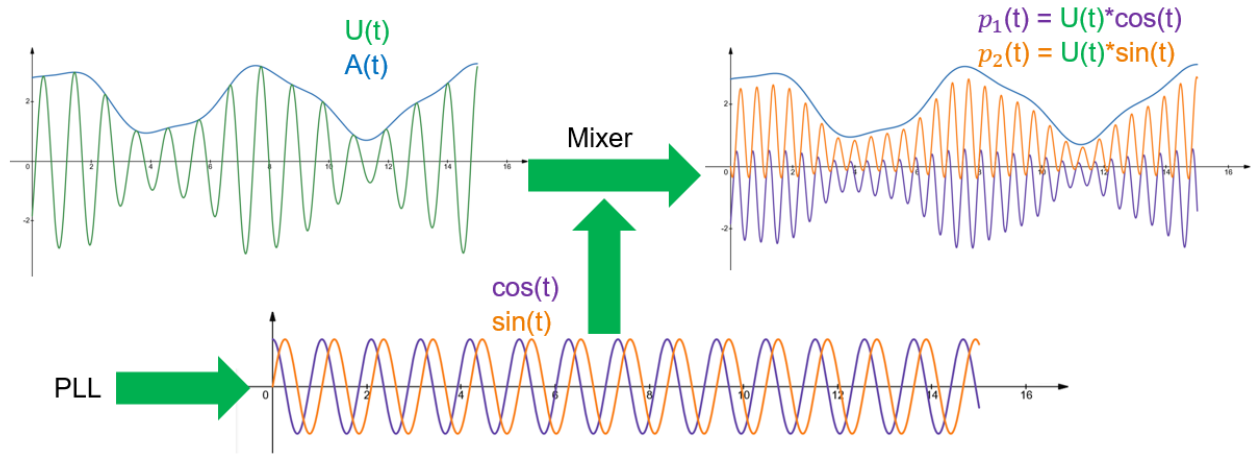


Figure 3.6: Lock-In Amplifier principle. Its aim is to recover the amplitude $A(t)$ and phase $\phi(t)$ of the response voltage $U(t)$. The Phase Locked Loop (PLL) generates a sine and cosine waveforms locked in phase with $U(t)$. The latter gets separately multiplied by the sine and cosine, producing the waveforms $p_{1/2}(t)$, which contain a $2 \cdot f_{ext}$ component.

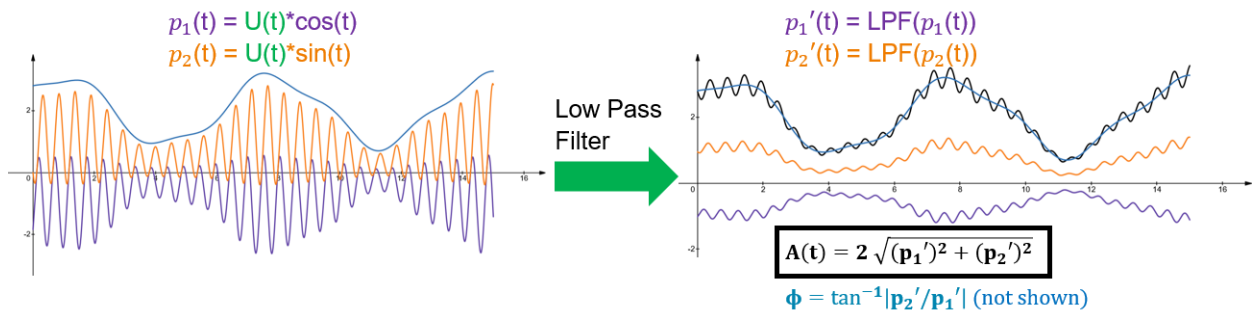


Figure 3.7: The second part of the LIA algorithm is the Low Pass Filter (LPF), which has to remove the $2 \cdot f_{ext}$ component from $p_{1/2}$, producing the filtered waveforms $p'_{1/2}$. To recover the amplitude $A(t)$ and phase $\phi(t)$ the black and azure formulas are used. A good LPF should remove as much of the residual excitation component as possible, leaving a good time resolution of the demodulated amplitude.

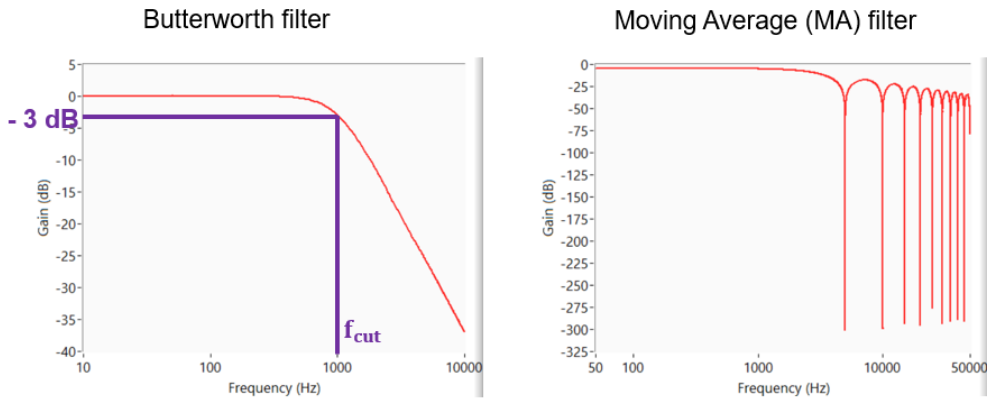


Figure 3.8: Bode plots showing frequency response of Butterworth filter and Moving Average.

The task of the LPF is to remove the $2 \cdot f_{ext}$ frequency component from the mixed waveforms $p_{1/2}$. If the LPF is not well tuned the resulting amplitude reconstruction $A(t)$ still contains this frequency component, as can be seen (exaggerated) in Fig. 3.7 (black plot). The LPF is also used to remove noise from the demodulated amplitude.

3.2.4 Low pass filter responses

There are many choices for low pass filters that can be used. An important part of this thesis concerned the investigation of different combination of filters to obtain the best signal quality and time resolution. The discussion here addresses digital low pass filters, since the Lock-In Amplifier has been implemented as digital algorithm on an FPGA. Digital filters perform arithmetic operations on the samples of a digital signal. They can perform different tasks like noise reduction or signal separation. Digital filters can be classified into two categories [16]: Infinite Impulse Response (IIR) filters and Finite Impulse Response (FIR) filters. This classification is based on how the filter reacts to an impulse, i.e. a signal that has a single non-zero sample. FIR filters have an impulse response that is limited to a finite number of samples; IIR filters, on the contrary, have an impulse response that lasts for an infinite number of samples. Filtering always costs in terms of time resolution of the signal. The stronger the LPF and the lower the noise, but the lower the time resolution of the signal becomes.

During the tests (see Chap. 4) a series of Moving Average (MA) and Butterworth filter have shown the best performance. A Butterworth filter is a low pass IIR filter that smooths signals above a certain frequency, creating a stopband. The cutoff frequency f_{cut} is defined as the frequency at which a signal is attenuated at - 3 dB.

A Moving Average is a FIR filter which performs an averaging over a number of samples MA_N .

Fig. 3.8 shows the frequency responses (Bode plots) for these two filters. The MA can totally eliminate one frequency (SR/MA_N) and its higher order harmonics. By tuning MA_N it is possible to very efficiently remove the $2 \cdot f_{\text{ext}}$ component from the demodulated LIA amplitude.

The Butterworth filter instead is used to remove noise above f_{cut} , which can also be tuned. This operation is particularly important when running the electronics in ASDEX Upgrade, where the electromagnetic interference is very high (see Sec. 4.2). If f_{cut} is too high the noise level remains too high. On the contrary, if f_{cut} is too low, the signal is over-smoothed and the time resolution is decreased.

A Lock-In Amplifier reconstructs the amplitude of a signal with known frequency (f_{ext} in the case of this thesis), ignoring the components at higher frequency, smoothed by the LPF. If there are noise sources with a frequency close to f_{ext} the LIA's output will be highly disturbed. Therefore, f_{ext} must be properly tuned in the bolometer cards.

Very low frequency noise sources also disturb the LIA's output, since they can't be totally removed by the LPF. Therefore it's important to characterize the noise of the working environment in order to be able to tune all the LIA's parameters.

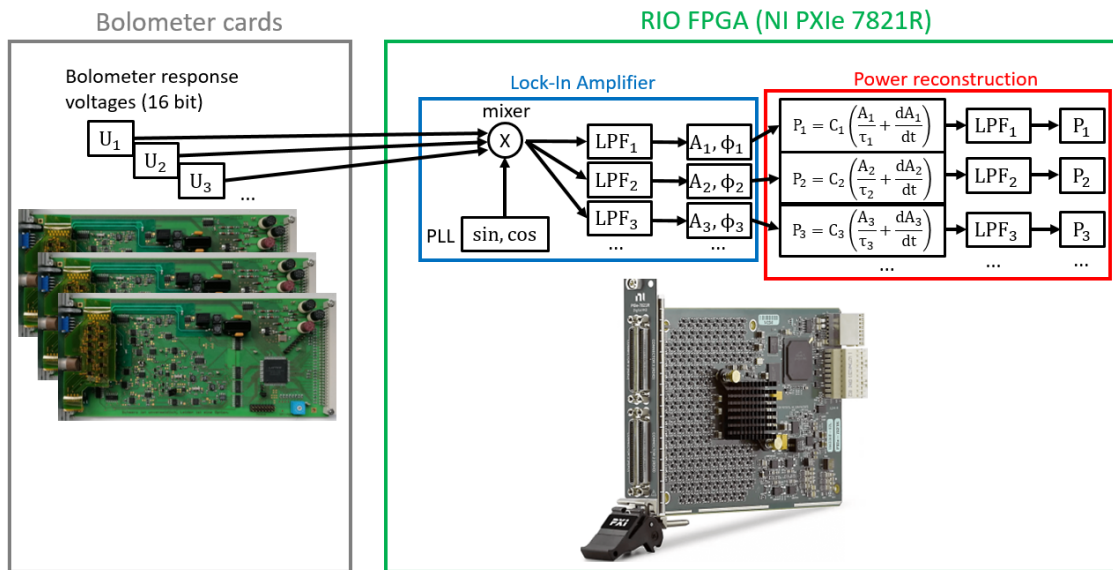


Figure 3.9: Simplified scheme of the firmware implemented on the RIO FPGA. The bolometer cards acquire the response voltages which are passed to the RIO FPGA. The Lock-In Amplifier performs amplitude reconstruction. From the LIA amplitudes the incident powers are reconstructed.

3.2.5 LIA and power reconstruction on RIO FPGA

Within this thesis a firmware for the RIO FPGA (see Sec. 3.2.2) has been developed, with the LabVIEW environment and its FPGA suite. The firmware implements the Lock-In Amplifier (LIA) algorithm for sinusoidal waveform and the incident power reconstruction, through eq. 2.1. The developed firmware can process up to four bolometer channels (i.e. one bolometer head) in parallel.

Lock-In Amplifiers exist both as analog and digital instruments. A digital LIA makes use of Digital Signal Processing (DSP) techniques and digital filters. In digital electronics a sinusoidal waveform $W(t)$ is a time series of points (samples) $W[i]$ acquired with a sampling rate (SR), which determines the time interval ($dt = 1/SR$) between every two samples. A sinusoidal waveform has a number of samples per period, which is the ratio between the SR and the waveform's frequency (f_{ext}). In digital electronics operations and filtering of waveforms become mathematical algorithms performed sample-by-sample. The speed of a digital algorithm depends on how many bits the operands have and how complex the operations to be performed are.

The base for the LIA algorithm on the RIO FPGA has been taken from [11] and adapted to the NI PXIe 7821R module. The function executed by the developed firmware is simplified in Fig. 3.9.

The frequency to which the LIA is sensitive can be adjusted. The PLL generates sine and cosine waveforms. For each bolometer channel, the response voltage U is multiplied by sine and cosine separately and the two new waveforms are low-pass filtered. There are many choices for the LPF. LabVIEW offers some basic digital filters for FPGA like Butterworth, Notch, Integrator, Decimator, FIR filters. The optimal LPF configuration found consists of a series of Moving Average and Butterworth filter (see Chap. 4). Amplitude A and phase ϕ are obtained through eq. 3.2, 3.3.

The demodulated amplitude A is used to perform the power calculation through eq. 2.1. The derivative of A is a particular concern because it amplifies the noise present in A . The derivative is calculated in the following way:

$$A'[i] = \frac{A[i] - A[i - k]}{k \cdot dt} = \text{SR} \cdot \frac{A[i] - A[i - k]}{k} \quad (3.4)$$

where k is an integer that can be chosen. Eq. 3.4 means that the derivative is calculated as a difference between two k -spaced samples. This is done in order to mitigate the noise. The time dt represents the time interval between every two samples, which is the reciprocal of the sampling rate SR .

The incident power on the bolometer is calculated as:

$$P[i] = C \left(\frac{A[i]}{\tau} + \text{SR} \cdot \frac{A[i] - A[i - k]}{k} \right) \quad (3.5)$$

where C , τ are provided to the RIO FPGA after executing the calibration. In order to reduce noise an additional Butterworth filter is used on P .

The following signals for each bolometer channel can be retrieved from the RIO FPGA: current, excitation V_{ext} , response voltage U , sine and cosine generated by the PLL, demodulated amplitude A , phase ϕ and power P . Fig. 3.10 shows a zoomed example of some signals: the response voltage U (green) and the cosine (purple), sine (orange) generated by the PLL.

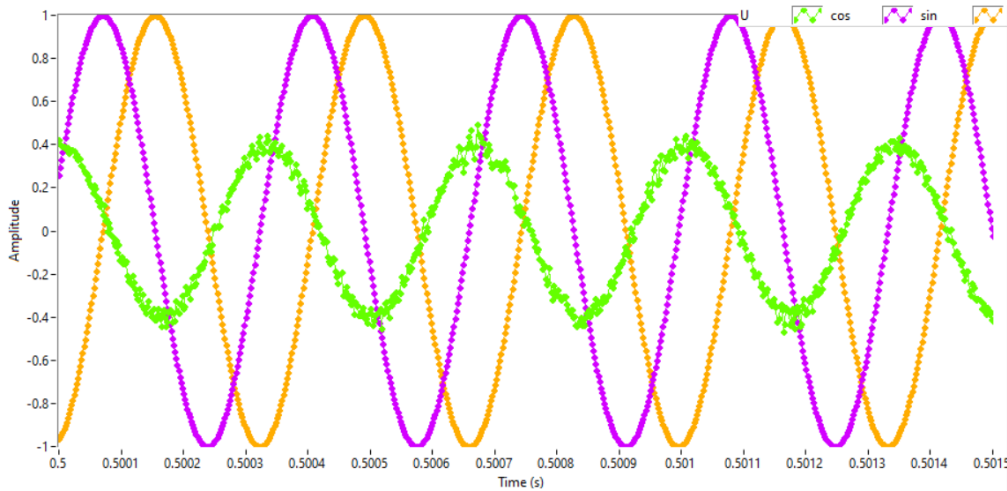


Figure 3.10: Example of waveforms, normalized to 1, from a DAQ run, with $SR = 500$ kHz, $f_{ext} = 2.976$ kHz (168 samples per period). The green signal is the response voltage U of one bolometer channel. The purple and orange ones are the cosine and sine waveforms generated by the PLL on the RIO FPGA and phase-locked to U .

3.2.6 Double frequency Lock-In Amplifier

A variation of the standard Lock-In Amplifier (LIA) has also been implemented on the RIO FPGA, using a double frequency excitation waveform. This waveform is obtained as the sum of two sinusoidal waveforms with defined frequencies and same amplitude. This allows to perform amplitude detection of both frequency components and allows to check if one of them is subject to particular noise.

The working principle is the same as the standard LIA algorithm, but here there are two LIAs that operate in parallel and each of them is sensitive to one frequency. With this method two amplitudes are detected. They are in principle identical, since they are both modulated by the same incident radiation. However, if there is a particular noise source that is close to one of them, the reconstructed amplitude will pick up this noise, while the other one will be clear. Fig. 3.11 shows an example of response voltage U of one bolometer channel with double frequency excitation waveform, with $f_{ext-low} = 2.976$ kHz, $f_{ext-high} = 50$ kHz.

This technique has been particularly important during the tests in the experimental campaign, in order to identify the best excitation frequency. However, it has not been chosen as final design, since the maximum amplitude of each frequency component is half the amplitude it would have alone.

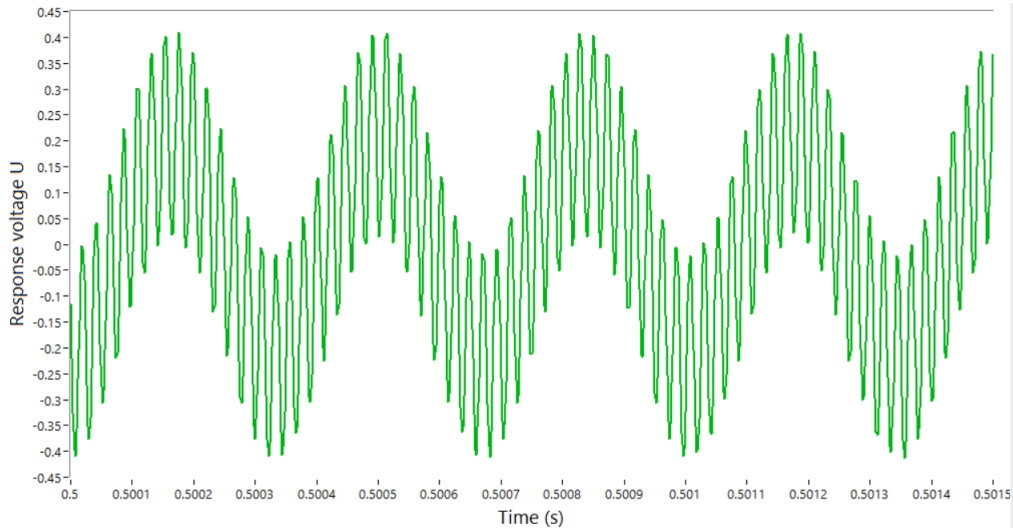


Figure 3.11: example response voltage U , normalized to 1, to double frequency excitation waveform, with $f_{\text{ext-low}} = 2.976$ kHz, $f_{\text{ext-high}} = 50$ kHz.

3.2.7 Resource and performance limits

Although the performance of the LIA algorithm has not been thoroughly investigated, it is worth mentioning that the developed firmware achieves real time capability on the RIO FPGA and supports SR up to 1 MHz, while the same algorithm on a computer takes several minutes to execute.

It has been observed that the RIO FPGA's resources usage (in terms of slices) scales approximately linearly, with a 10% increase for every channel added. With four bolometer channels handled in parallel, the FPGA resources usage (in terms of slices) is around 60%. This means that 100% would be reached with 8 channels and it won't be possible to handle more than this in parallel. A possible solution, not investigated in this thesis, is to store all the ADC data in the FPGA memory and apply the LIA algorithm sequentially to each channel.

A time limiting factor has been found on the side of the interface cards, which manage the communication between the bolometer cards and the RIO FPGA. When increasing the number of bolometer cards connected, it has been observed that the interface card is unable to retrieve the ADC samples at high SR. In particular with one card the SR can go up to 1 MHz, which is the maximum supported by the ADCs. With a higher number of cards the SR is limited to 500 kHz. This is a data communication problem: the ADCs in the bolometer cards can sample up to 1 MHz, but the interface cards have a limited data rate and can transmit it at maximum 500 kHz.

It is good practice to have at least 10 samples per waveform period. For this reason waveforms with maximum $f_{\text{ext}} = 50$ kHz have been used in the tests conducted.

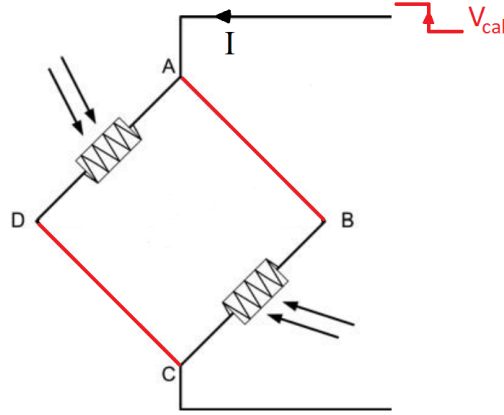


Figure 3.12: Wheatstone bridge with the two passive resistors short-circuited for the calibration procedure. A voltage step V_{cal} is applied and the current response I is measured.

3.3 Calibration of foil bolometers

The calibration procedure is used to evaluate the constants C , τ for each bolometer channel, in order to perform the incident power calculation through eq. 2.1:

$$P_{in} = C \left(\frac{U}{\tau} + \frac{dU}{dt} \right)$$

C [J/V], τ [s] are related to the thermal properties of the bolometer foils.

In the calibration procedure two resistors, belonging to the same foil (either masked or exposed) are short-circuited and excluded from the Wheatstone bridge, as shown in Fig. 3.12. This is implemented by relays on the bolometer cards. A current is driven by a defined voltage step V_{cal} on the remaining resistors. This current heats up the foil and, therefore, also changes the resistance. The time evolution of the current transient is shown in Fig. 3.10, and can be fitted by an exponential function:

$$I(t) = \Delta I \cdot e^{-t/\tau} + I_0 \quad (3.6)$$

which gives the transient amplitude ΔI , cooling time τ , equilibrium current I_0 . Assuming that the two non short-circuited resistors have equal resistance, their value can be found with Ohm's law:

$$R = 2 \cdot \frac{V_{cal}}{I_0} \quad (3.7)$$

where the factor 2 is present because each resistor is crossed by a current $I/2$. The resistance of the 40 m cables ($2 \Omega/m$) has to be subtracted to eq. 3.7.

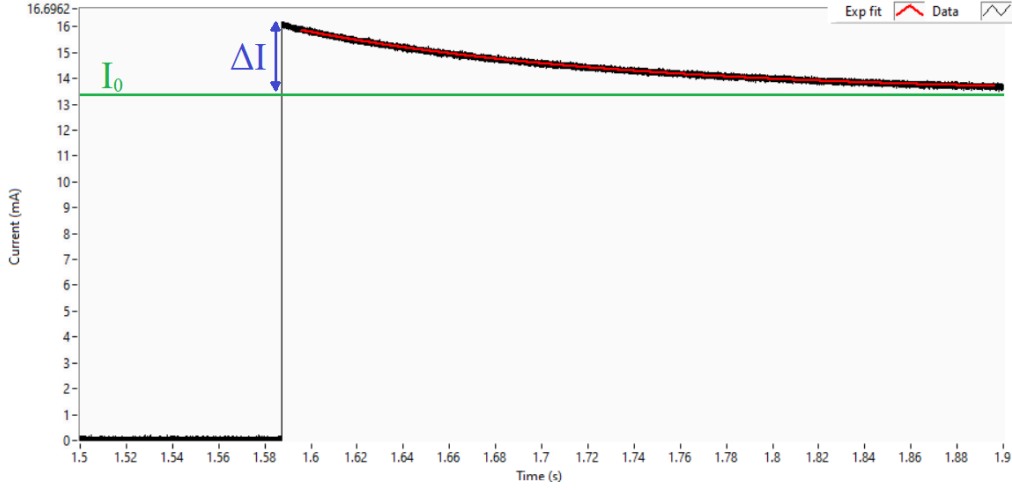


Figure 3.13: current transient during calibration procedure. A 10 V step is applied at $t = 1.59$ s to the exposed resistors. The current I (black) is fitted with an exponential (red) over 0.3 s.

The normalized heat capacity of the foil is defined as [8]:

$$\kappa_M[\text{W}/\Omega] = \frac{R \cdot I_0^4}{4 \cdot V_{\text{cal}} \cdot \Delta I} \quad (3.8)$$

from which the constant C can be obtained as:

$$C[\text{J}/\text{V}] = \frac{2 \cdot R \cdot \tau \cdot \kappa_M}{|V_{\text{ext}}|} \quad (3.9)$$

where $|V_{\text{ext}}|$ is the amplitude of the excitation waveform used in measurement mode. This calibration procedure is exploited by the present bolometer electronics at ASDEX Upgrade, which induce a 2.5 V step across the Wheatstone bridges. The calibration procedure is executed in the time between AUG's plasma discharges, documenting the calibration constants for every discharge.

The new electronics can perform the same procedure and allow to set the voltage step and which resistors are short-circuited. Fig. 3.13 shows an example of calibration with the new bolometer cards. A voltage step of 10 V is applied at $t = 1.59$ s and the current response is fitted, in post processing, with an exponential function. The results are the following: $\Delta I = 2.46$ mA, $I_0 = 13.40$ mA, $\tau = 140.6$ ms. From these values the following are obtained: $R = 1.4$ k Ω , $\kappa_M = 0.45$ mW/ Ω , $C = 12$ mJ/V.

The calibration procedure with the new electronics performs very similarly to the present electronics and can be used in between AUG's plasma discharges. However, the new system tends to underestimate the value of τ by $\approx 20\%$, for reasons probably related to the use of a higher calibration voltage than in the present bolometry electronics.

Chapter 4

New bolometry electronics tests

This chapter presents the tests of the new electronics and the Lock-In Amplifier (LIA) and power reconstruction algorithm implemented on the RIO FPGA. Some tests have been executed in the laboratory, with an artificial light source and an optical chopper with adjustable frequency, in order to evaluate the time resolution achievable. Subsequently the system has been tested in the latest ASDEX Upgrade experimental campaign, started in October 2024.

4.1 Tests in the laboratory

A bolometer head and four bolometer cards have been tested in the laboratory. The experimental setup is shown in Fig. 4.1. The bolometer head is placed in front of a light source with fixed intensity, with an optical chopper in between. The chopper's rotational speed can be tuned in order to create an intermittent light with adjustable frequency f_{chop} . This allows to test what the time resolution is, i.e. the maximum chopper frequency that can be resolved by the electronics. Different light sources have been used and a 1 mW red laser (650 nm wavelength) has taken as reference. With this method the incident power signal is a square wave, since a chopper allows either light or dark. The electronics have been run with sinusoidal excitation waveform with frequency f_{ext} . The Lock-In Amplifier algorithm on the RIO FPGA has been run with a Moving Average (MA) with adjustable sample width MA_N , followed by a Butterworth low pass filter with cutoff frequency f_{cut} .

The LabVIEW interface, run on a laptop, allows to adjust the following parameters, passed to the RIO FPGA:

- Sampling Rate SR (max 500 kHz to run more cards in parallel);
- DAQ duration in seconds;
- excitation frequency f_{ext} (max 50 kHz);

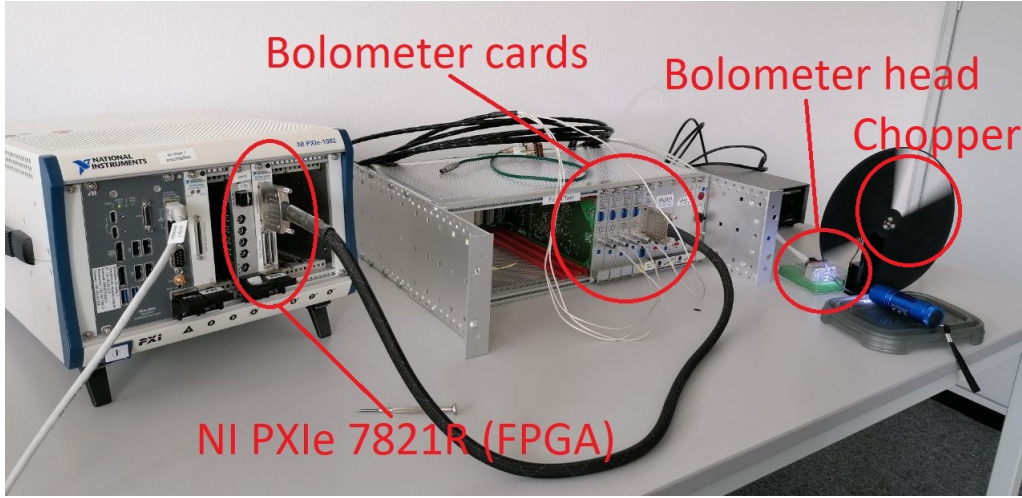


Figure 4.1: test setup used in the laboratory: a light source (torch or red 1 mW laser) with an optical chopper illuminate a bolometer head (4 channels). The head is connected to the bolometer cards which communicate, through an interface card, with the NI PXIe 7821R module embedding the RIO FPGA.

- excitation amplitude voltage $|V_{\text{ext}}|$ (only 20 V used);
- moving average samples MA_N ;
- cutoff frequency f_{cut} of Butterworth filter;
- k factor for derivative (see Sec. 3.2.5);
- cutoff frequency $f_{\text{cut,D}}$ of the Butterworth filter applied to the power signal;
- C and τ (obtained from previous calibration).

The measurements performed are aimed at characterizing the signal to noise ratio (SNR) and time resolution of the reconstructed incident power, achieved with the different LIA parameters and settings. The SNR is calculated in decibels with the following formula:

$$\text{SNR} = 20 \cdot \log_{10} \left(\frac{S}{N} \right) \text{ dB} \quad (4.1)$$

where S, N are amplitudes of signal and noise. When the SNR is negative the signal cannot be resolved.

S is approximated with the maximum variation of the demodulated amplitude or calculated power, as shown in Fig. 4.2, 4.3. With this definition S for the LIA amplitude depends on the light source used and on the duration of the light pulse. The SNR calculated with this approximation is valid within this thesis since the same light source has

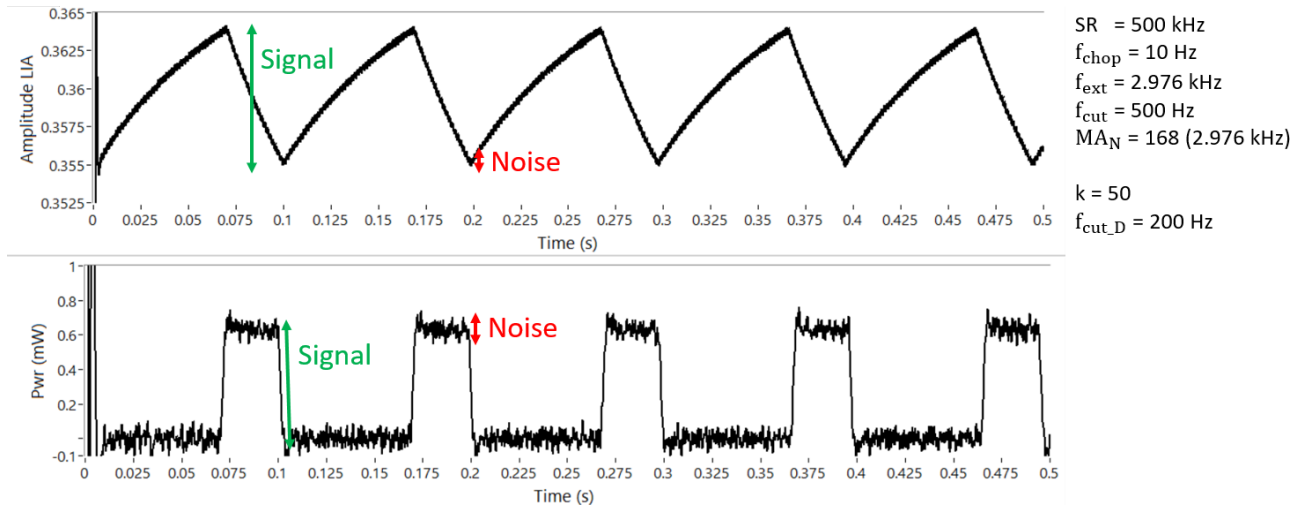


Figure 4.2: 0.5 s DAQ run with 1 mW laser and $f_{\text{chop}} = 10$ Hz. The DAQ parameters are listed on the top right. Top plot: demodulated amplitude; bottom plot: incident power [mW]. $\text{SNR}(\text{LIA}) = 38$ dB; $\text{SNR}(\text{Pwr}) = 24$ dB.

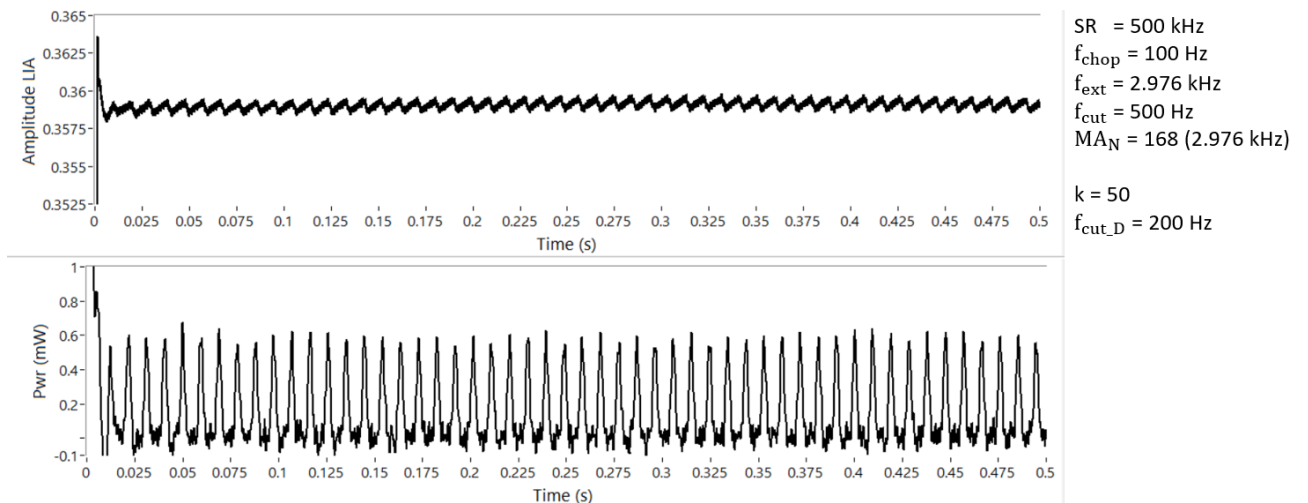


Figure 4.3: 0.5 s DAQ run with 1 mW laser and $f_{\text{chop}} = 100$ Hz. The DAQ parameters are listed on the top right. Top plot: demodulated LIA amplitude; bottom plot: incident power [mW]. $\text{SNR}(\text{LIA}) = 16$ dB; $\text{SNR}(\text{Pwr}) = 20$ dB.

been used, but cannot be used for comparison with other systems.

The noise amplitudes are evaluated as standard deviations over 50000 samples (0.1 s, given $SR = 500$ kHz) of a DAQ run without any incident light. For the LIA amplitude, normalized to 1, $N = 0.00008$ was obtained. For the reconstructed power $N = 0.04$ mW was found, which is the power resolution of the system, i.e. the lowest measurable incident power. For the response voltage the noise level was calculated from a DAQ run with 0 V applied to the bridge and it was obtained $N = 20$ ADC units, which corresponds to 6 mV on the ± 10.24 V ADC scale.

Fig. 4.2, 4.3 show two DAQ runs of 0.5 s with a single bolometer channel, respectively with 10 Hz and 100 Hz laser chopping frequencies. The top plot is the demodulated LIA amplitude, from which the incident power (bottom plot) is obtained through eq. 2.1 as explained in Sec. 3.2.5. The LIA amplitude is normalized to 1. In the top right of each figure the DAQ and LIA parameters are listed. The Moving Average samples width MA_N is adjusted in order to remove the excitation frequency from the demodulated LIA amplitude (see Sec. 3.2.4). Next to MA_N the corresponding removed frequency is reported.

The laser power reconstructed by the electronics is lower than 1 mW because the laser beam's area is larger than the bolometer foils and the beam is partially reflected.

S decreases as the chopping frequency increases, while N remains constant. This means that SNR also decreases when f_{chop} increases and it becomes more difficult to resolve faster signals. This is due to the heating and cooling curves, with a time constant τ , that the bolometer foils undergo when subjected to a steep power transient.

From a linear extrapolation, the SNR of the LIA amplitude was found to approach 0 dB at $f_{chop} \approx 200$ Hz, representing the fastest signal that can be resolved. This results in a time resolution of ≈ 5 ms. This value outperforms the present bolometer electronics, which achieve a time resolution of ≈ 15 ms (66 Hz).

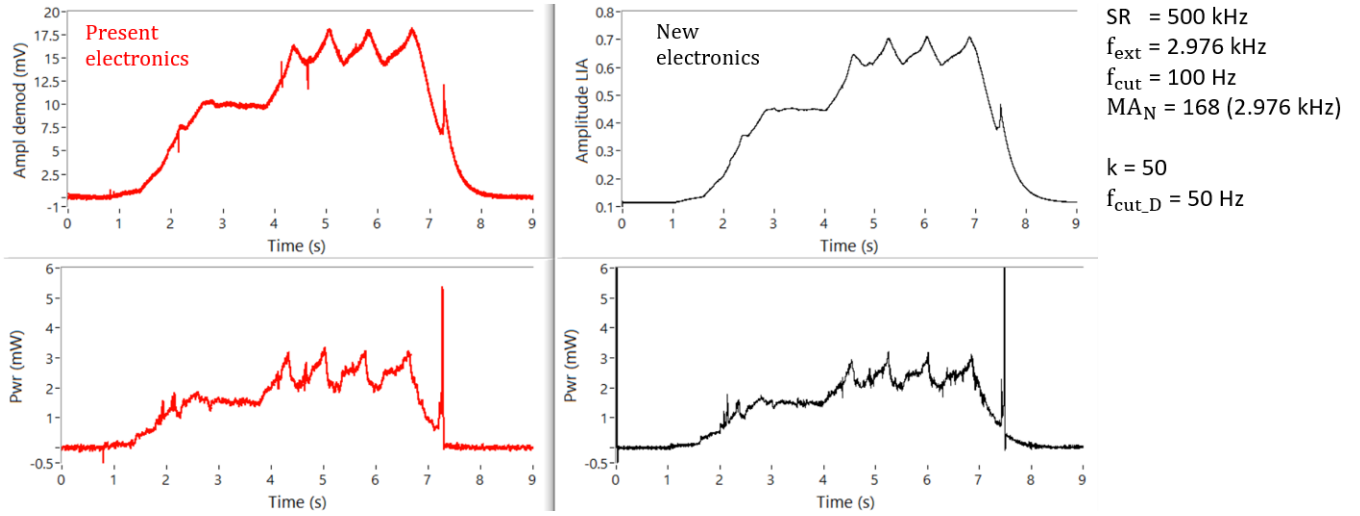


Figure 4.4: Example DAQ run of one bolometer line of sight during an AUG plasma discharge, acquired with the present bolometry electronics (red, on the left) and the new one with the optimal parameters (black, on the right). Top plots: demodulated amplitudes (the LIA is normalized to 1); bottom plots: reconstructed incident powers. At the top right the main DAQ parameters of the new electronics are listed. $N_{\text{pwr-new}} = 0.03 \text{ mW}$, $N_{\text{pwr-pres}} = 0.04 \text{ mW}$.

4.2 Tests in the latest AUG campaign

In October 2024 the experimental campaign at ASDEX Upgrade restarted, after a two-year construction and maintenance phase of the tokamak. The new bolometer electronics have been run from November 2024 to January 2025 and tested with real AUG plasma discharges. This part of the testing is very important, since the conditions during a plasma discharge are very different from the conditions of a laboratory. In particular, this phase allowed to test the new electronics with the long 40 m cables and the noise induced by the intense magnetic fields and the different systems required for the tokamak's operation.

The signals obtained with the new electronics have been compared to the ones obtained with the present electronics, which exploit a 2.5 kHz square excitation (See Sec. 3.1). The goal is to evaluate if the new system brings an improvement in time resolution and level of noise. The electronics have been tested with one bolometer line of sight of the F01 camera (see Fig. 2.4). Since there are multiple F01 cameras, in different toroidal positions inside AUG, it is possible to acquire data for the same line of sight both with the present bolometry electronics and with the new one, to directly compare them. The DAQ is controlled through a LabVIEW interface and is triggered by the integrated discharge control system of AUG, 1 s before the plasma is started. Each DAQ run lasts 12

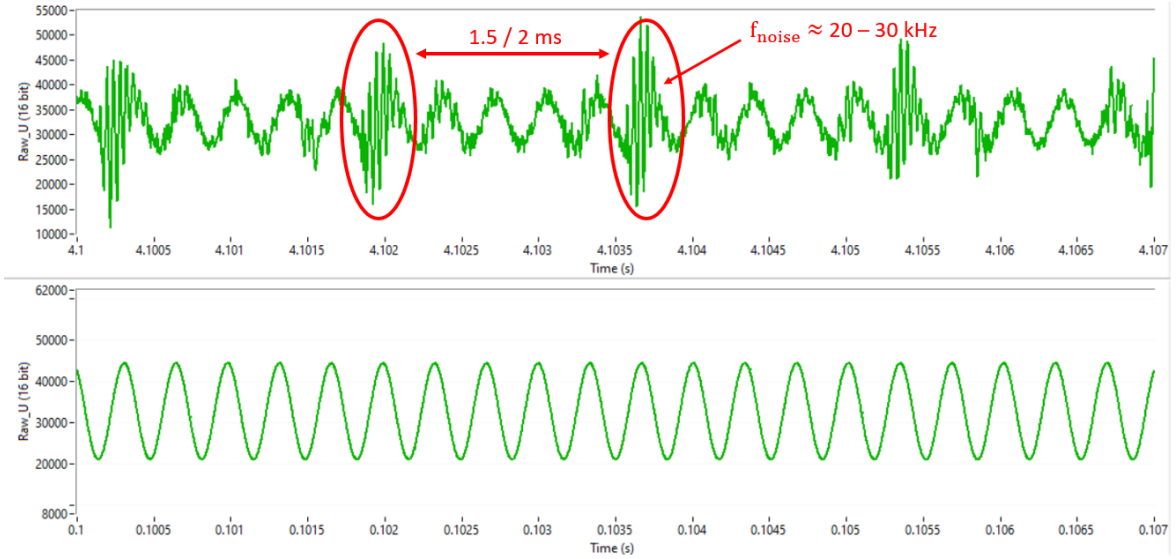


Figure 4.5: comparison of the response voltage U with $f_{\text{ext}} = 2.976$ kHz in AUG (top plot) and in the laboratory (bottom plot). The values are 16 bits integers from the ADC. A distinctive noise source occurring every $1.5/2$ ms is found in AUG. This noise source is probably related to the switching of some power supplies for the magnetic coils.

s, sufficient to record an entire plasma duration of max 10 s.

The tests of the new electronics characterized how the excitation frequency f_{ext} and the low pass filter parameters for the LIA algorithm and power reconstruction affect the performance. All DAQ runs shown were performed with a series of Moving Average (MA) with MA_N samples width and Butterworth filter with cutoff frequency f_{cut} for the LIA LPF and an additional Butterworth filter with cutoff frequency $f_{\text{cut,D}}$ to smooth the power signal.

Decreasing f_{cut} and $f_{\text{cut,D}}$ implies that a stronger filtering is applied, which decreases noise but also lowers the time resolution.

The MA filter was always tuned to remove the $2 \cdot f_{\text{ext}}$ residual frequency component from the LIA signal (see Sec. 3.2.3), by setting MA_N equal to the number of samples per period of the excitation waveform ($N_{\text{wfm}} = SR/f_{\text{ext}}$). It is worth noting that setting $MA_N = N_{\text{wfm}}/2$ also works, since the residual frequency to be removed from the LIA signal is double the excitation frequency. However, choosing $MA_N = N_{\text{wfm}}$ has proven to be more accurate in removing this frequency. This is equivalent to saying that the Moving Average integrates over two periods of the $2 \cdot f_{\text{ext}}$ component. It is also worth remembering that the Moving Average removes all the higher order harmonics of a base frequency ($= SR/MA_N$). In the shown plots, next to MA_N , the value of the lowest frequency removed by the MA is reported.

The integer factor k for the derivative calculation (see Sec. 3.2.5) was adjusted in the

range [10, 50], showing that a higher value gives less noisy reconstructed power. The tests allowed to find an optimal set of the aforementioned parameters:

- $f_{\text{ext}} = 2.976$ kHz;
- $f_{\text{cut}} = 100$ Hz;
- $MA_N = 168$ (2.976 kHz);
- $k = 50$;
- $f_{\text{cut.D}} = 50$ Hz.

These parameters allowed to obtain a noise level and time resolution comparable to those achieved by the present bolometry electronics. No significant improvement was found. The reasons will be discussed in the following.

Fig. 4.4 shows an example DAQ run of one bolometer channel during a plasma discharge, acquired with the present bolometry electronics (in red on the left) and with the new electronics with the optimal parameters (in black on the right). The top plots show the demodulated amplitudes: in mV for the present electronics and normalized to 1 for the new ones. The bottom plots show the reconstructed incident power, in mW. The values of the demodulated amplitudes (upper plots) cannot be directly compared, since they are expressed with different units and since the bolometers have different thermal constants C , τ . However, a qualitative analysis shows that the relative noise floor is lower for the new electronics. From the plots shapes it can be observed that the new electronics measure the same signals as the present electronics, showing that the new system can be used during tokamak's operation.

The shapes of the reconstructed powers have some differences. Firstly, the peak at $t = 7.5$ s (plasma disruption) is lower in the left plot. This is related to the fact that in the present electronics a stronger filtering is used, which attenuates noisy peaks but also disruption peaks, underestimating their radiated power. Secondly, the right plot takes some time to reach zero after the disruption peak, unlike the left one. This is due to the calibration constants, particularly τ , which are not perfectly measured by the new electronics (see Sec. 3.3).

For every DAQ run the noise level N_{pwr} of the reconstructed power signals is evaluated as standard deviation over the first 0.5 s, where no radiation is present. This figure of merit is used to compare the different DAQ runs. For this run it was found $N_{\text{pwr-new}} = 0.03$ mW, $N_{\text{pwr-pres}} = 0.04$ mW. The two systems achieve a very similar noise level, but the cutoff frequency of the power signal in the right plot is 50 Hz, limiting the time resolution to ≈ 20 ms, which is comparable to the one of the present system and does not bring a significant improvement.

The tests evidenced a higher noise level than in the laboratory, as expected. The noise in the reconstructed power signal comes from the noise in the raw U signal, which is much higher than that observed in the laboratory. Fig. 4.5 shows a comparison of the response voltage U , expressed as 16 bit integers from the ADC, with $f_{\text{ext}} = 2.976$ kHz, in the laboratory (bottom plot) and during an AUG discharge (top plot). In the latter case the sinusoidal waveform is highly distorted.

A particular noise source was found and is evidenced in red in Fig. 4.5. This noise occurs very regularly every 1.5 - 2 ms (500 - 600 Hz) with an oscillation frequency around 20 - 30 kHz. This noise appears approximately 4 s before the plasma is started and stops just after the discharge's end. The origin of this noise source has not been fully identified and has been recorded by the AUG team since November 2024, from the campaign's start, also in other diagnostic systems. With high probability, it is related to the switching of the power supplies of the magnetic field coils, which convert AC to a controlled DC output and operate on a frequency of 500 - 700 Hz. These power supplies induce voltage spikes picked up by the long bolometer cables. The oscillation frequency around 20 - 30 kHz is probably the result of the cables response to the voltage spikes, which cause resonances whose frequency depends on the cables length.

The noise level over the response voltage was calculated as standard deviation of a DAQ run with 0 V applied to the bridge, in order to avoid any signal and visualize the pure noise. The noise level calculated between two switching events is $N \approx 500$ ADC units (≈ 150 mV on the ± 10.24 V ADC scale). The noise level, calculated including also the switching events, increases to $N \approx 3000$ ADC units (≈ 900 mV on the ADC scale).

Without considering the switching events, the noise level in AUG is more than an order of magnitude higher than in a laboratory environment, where it was measured to be $N \approx 20$ ADC units (≈ 6 mV on the ADC scale, see Sec. 4.1). This implies a lower achievable SNR with respect to the laboratory and a stronger LPF required (lower cutoff frequencies).

It was found that the excitation frequency f_{ext} must be outside of the frequency range [20 - 30] kHz, otherwise the LIA algorithm amplifies also the noise. One can either use a higher or lower excitation frequency. Fig. 4.6 (on the right) shows a DAQ run with frequency $f_{\text{ext}} = 25$ kHz, which falls within the range [20, 30] kHz. The noise level of this DAQ run is very high and no clear shape in the power signal can be identified, when compared to the present electronics. At the end of the plasma discharge, around $t = 6.9$ s a drastic noise reduction is clearly visible. This is the point where the switching noise stops.

The noise amplitude in the reconstructed power signal is $N_{\text{pwr}} = 0.72$ mW, much higher than $N_{\text{pwr-pres}} = 0.03$ mW.

Using a high excitation frequency ($f_{\text{ext}} > 30$ kHz) was found to be inefficient for different reasons. Firstly, the number of samples per waveform period is low. For example, with

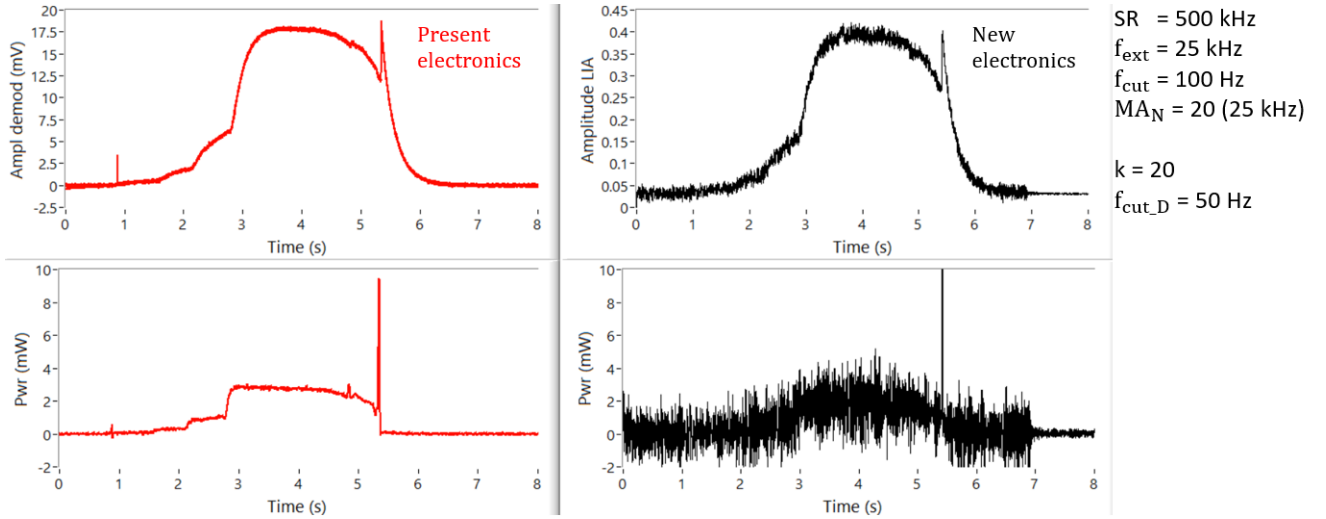


Figure 4.6: DAQ run with $f_{ext} = 25$ kHz, which is in the range of the power supply's noise source, therefore producing a very noisy LIA output and power. $N_{pwr-new} = 0.72$ mW, $N_{pwr-pres} = 0.03$ mW.

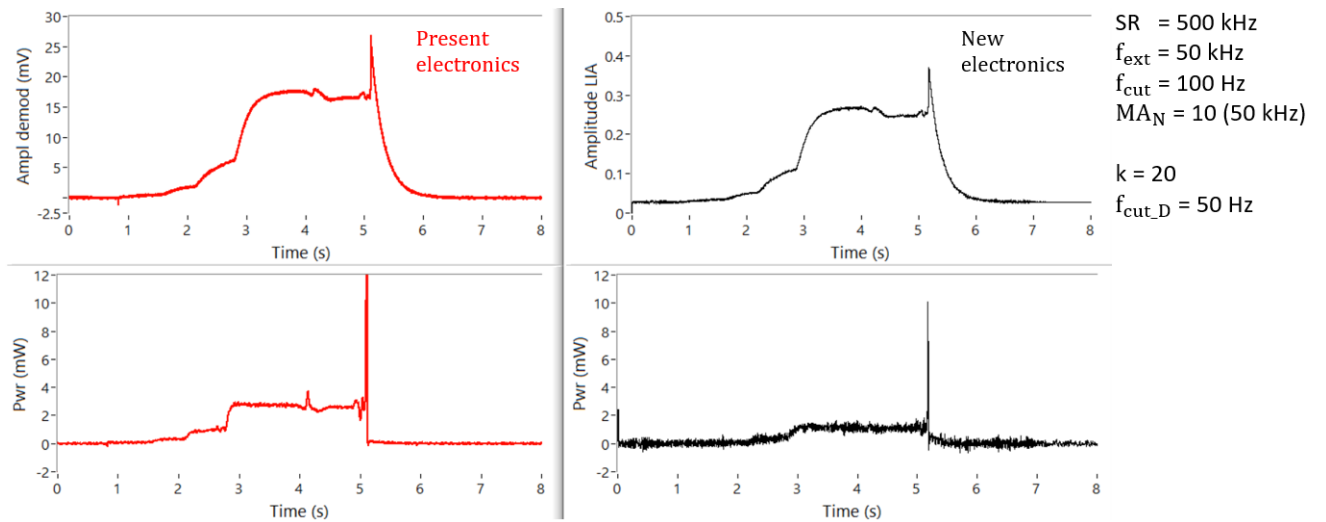


Figure 4.7: DAQ run with $f_{ext} = 50$ kHz. The power measured by the new electronics underestimates the one measured by the present electronics. The reason is attributed to the long connecting cables that act as low pass filters and attenuate the 50 kHz excitation. $N_{pwr-new} = 0.20$ mW, $N_{pwr-pres} = 0.04$ mW.

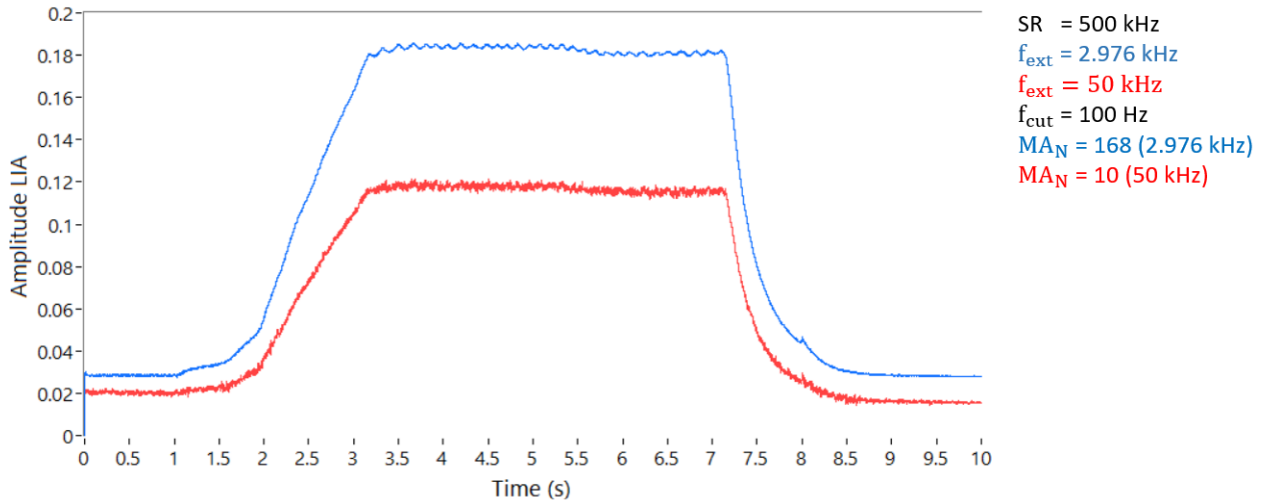


Figure 4.8: DAQ run performed with double frequency excitation waveform with $f_{\text{ext-low}} = 2.976$ kHz, $f_{\text{ext-high}} = 50$ kHz. Only the demodulated LIA amplitudes are shown. The higher frequency amplitude (red plot) is attenuated by 33% with respect to the lower frequency one (blue plot). The cause for this has been partially attributed to the attenuation by the long bolometer cables.

$f_{\text{ext}} = 30$ kHz and $\text{SR} = 500$ kHz the ADCs produce ≈ 16 samples per period. The noise reduction with such high frequency excitations was found to be not as good as with low frequency excitations (< 5 kHz).

Secondly, it was found that, with a high frequency excitation, the reconstructed power signal is systematically attenuated. Fig. 4.7 shows this phenomenon, through a DAQ run acquired with $f_{\text{ext}} = 50$ kHz (10 samples/period). The reconstructed power, with the new electronics, underestimates the power measured with the present electronics, by $\approx 50\%$. The reason for this probably lies in the long cables that connect the bolometers to the electronics and act as low pass filters, attenuating the high excitation frequency. As discussed in [8], the 40 meter bolometer cables have $2 \Omega/\text{m}$ series resistance and about 2 nF parasitic capacitance. A bolometer channel has equivalent resistance ≈ 1.3 k Ω . The cable acts as an RC low pass filter with cutoff frequency $f_{\text{cable}} = 1/(2\pi RC) \approx 60$ kHz. This means that frequencies in the range [30, 50] kHz are attenuated by 10% - 25%.

This phenomenon was evidenced also by the tests performed with the double-frequency excitation waveform (see Sec. 3.2.6 for explanation). Fig. 4.8 shows a DAQ run performed with an excitation V_{ext} with two frequencies: 2.976 kHz, 50 kHz (see also Fig. 3.11). The image shows the two demodulated LIA amplitudes. The amplitude of the high frequency component (red) is approximately 33% lower than the amplitude of the low frequency component (light blue). This is partially compatible with the discussed hypothesis of cables attenuation. However, there could be another unknown effect which

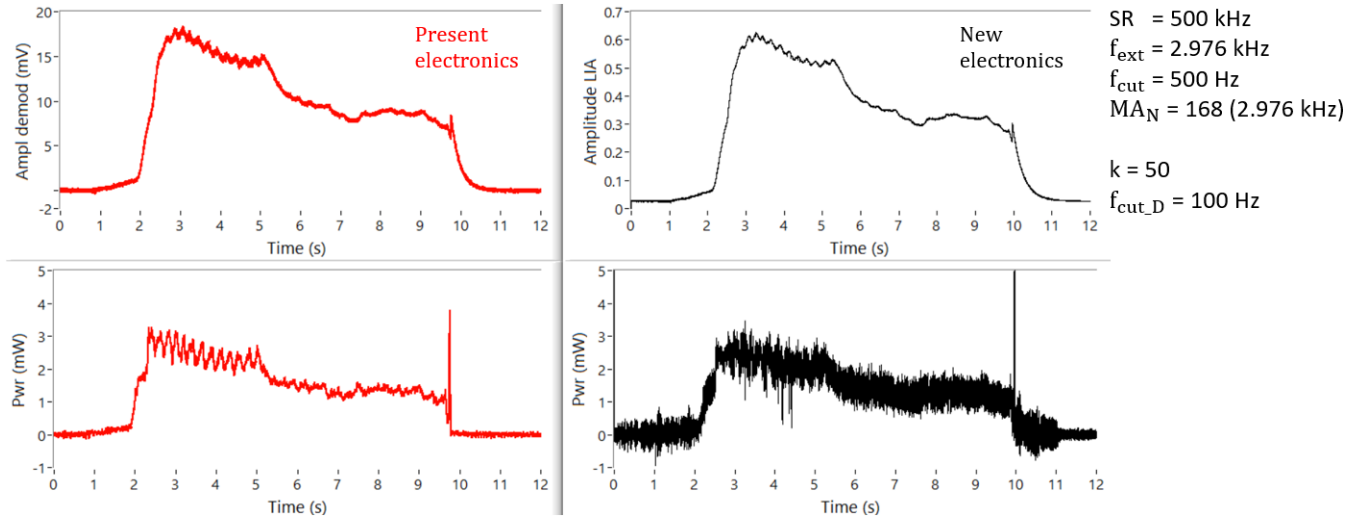


Figure 4.9: DAQ run with $f_{\text{ext}} = 2.976$ kHz, $f_{\text{cut}} = 500$ Hz, $f_{\text{cut}_D} = 100$ Hz. The increased cutoff frequency increases the noise floor and does not improve the time resolution. $N_{\text{pwr-new}} = 0.21$ mW, $N_{\text{pwr-pres}} = 0.04$ mW.

causes further attenuation of high frequencies.

Tuning the excitation frequency has proven to be an important factor for improving the signals. The previously discussed tests led to lower the excitation frequency and choose $f_{\text{ext}} = 2.976$ kHz.

Some tests with increased cutoff frequencies were also performed. One example is shown in Fig. 4.9, with $f_{\text{cut}} = 500$ Hz, $f_{\text{cut}_D} = 100$ Hz. The increased cutoff frequency reduces the attenuation of strong signals like the plasma disruption, at $t = 10$ s. However, it is unable to bring a better time resolution because it also drastically increases the noise floor. In particular, the fast radiation pattern from $t = 2.5$ s to $t = 5$ s is not resolved in the right plot. For this DAQ run it was found $N_{\text{pwr-pres}} = 0.04$ mW, $N_{\text{pwr-new}} = 0.21$ mW.

The tests performed during the latest AUG campaign generally showed that the demodulated bolometer amplitude with the new electronics can achieve lower noise level than the present electronics, provided the excitation frequency f_{ext} is out of the range [20, 30] kHz. The main issue of the new electronics is the derivative calculation implemented to obtain the power signal. It was not possible to drastically reduce the noise level of the power signals under the present system's level, even with strong low pass filtering. The time resolution was not drastically improved. Using more sophisticated techniques, like Savitzky Golay filtering or polynomial fitting could bring better performance.

The tests showed that the measurements are dominated by the noise produced by the tokamak's systems. In the laboratory the new electronics can resolve fast signals up to

200 Hz, while they are limited to ≈ 50 Hz in the tokamak's environment.

The performance is expected to improve if the noise from the coils power supplies is removed. However, even without this noise source, the noise level is more than an order of magnitude higher than in the laboratory and the performance in the tokamak's environment is expected to be worse than in the laboratory.

With the new electronics it is possible to characterize the noise sources, thanks to the possibility of sampling the full waveform period with SR up to 500 kHz (1 MHz if a single channel is used). This is not possible with the present system, since the AD7730 chips don't allow to record the raw bolometers response voltages.

The new electronics bring a great flexibility and allow to explore a wide range of parameters and noise reduction techniques. Tuning the excitation frequency or producing double-frequency excitations, for example, showed to be crucial features to obtain better measurements.

Many other filter configurations and firmwares on the RIO FPGA can be explored. For example, a firmware to detect and suppress the 20 - 30 kHz noise; a firmware to calculate the derivative in a more efficient way (e.g. Savitzky Golay filter); a firmware with a demodulation technique other than Lock-In Amplifier. Testing a square excitation would also be worth trying, to have a similar system to the present one.

The new electronics allowed to create a flexible DAQ system for foil bolometry, where both voltage measurement and power reconstruction are performed online, without the need of an external computer for post-processing analysis, as instead is done with the present electronics.

Chapter 5

Summary and outlook

This thesis focused on the implementation of new electronics for foil bolometry: a diagnostic technique used in nuclear fusion machines to measure the total electromagnetic power radiated by plasmas, ranging from near infrared to soft X-rays.

Within this thesis new electronics for foil bolometry at the ASDEX Upgrade (AUG) tokamak have been implemented and tested, both in the laboratory and in the latest AUG experimental campaign, from October 2024 to January 2025. The results obtained with the new electronics have been compared to the ones obtained with the existing electronics, already in operation at AUG.

The new electronics comprise new bolometer cards developed in-house at Max Planck Institute for Plasma Physics (IPP) and interfaced to a National Instrument (NI) module that embeds an FPGA.

The new bolometer cards allow to produce several types of excitation waveform for the Wheatstone bridges in the bolometers, as opposed to the present electronics which work with a fixed 2.5 kHz square waveform. The new electronics allow to acquire the full waveform period and to perform different amplitude demodulation techniques to recover the bolometers' response voltage amplitudes and perform incident power calculation.

In particular this thesis focused on implementing an amplitude demodulation algorithm with sinusoidal excitation waveform, with the goal of improving time resolution and reduce noise in the bolometer power signals. The chosen algorithm is the Lock-In Amplifier (LIA). The demodulated LIA amplitudes of the bolometers are used to perform incident power reconstruction. With the LabVIEW software, and its FPGA suite, a firmware for the NI FPGA has been developed. The firmware implements the LIA and power reconstruction algorithm in real time, for maximum four bolometer channels.

The DAQ chain, composed by bolometer heads, bolometer cards and NI FPGA has been preliminarily tested in the laboratory. A 1 mW red laser has been chosen as reference signal. An optical chopper allowed to create signals with adjustable frequency, to test the time resolution achievable with the new electronics. The analysis showed that the time resolution is around 5 ms (200 Hz) for a 1 mW signal, which overcomes the present

bolometry electronics, which has time resolution around 15 ms (66 Hz).

Subsequently the new electronics have been tested during the latest AUG experimental campaign. The tests aimed at finding the best parameters for the LIA algorithm. The tests evidenced a much higher level of noise, more than an order of magnitude than in a laboratory environment. A specific noise source, within the range of [20, 30] kHz, probably related to some power supplies that act during the tokamak's operation, was found but its source was not clearly identified. It was found that decreasing the excitation frequency f_{ext} of the sinusoidal waveform helps reducing noise and achieve higher time resolution. An optimal low pass filter configuration for the LIA algorithm was found. This consists of a series of Moving Average, used to remove the residual excitation frequency from the LIA signal, and Butterworth filter, used to reduce noise. The signals obtained with the new electronics do not show a significant improvement in time resolution with respect to the ones obtained with the present electronics. The cause of this has been identified with the high level of noise during the tokamak's operation.

The new electronics, however, helped to identify this issue, thanks to the capability of recording the full waveform period, which is not possible with the present bolometry electronics.

To conclude this work, the new bolometry electronics proved to be very performing in the laboratory, showing low noise level (≈ 20 ADC units) and ability to resolve fast signals. The strength of the new electronics is the flexibility: many types of excitation waveforms with adjustable frequency can be induced and the NI FPGA can process data in real time and provide calculation for the incident power. This allowed to create a DAQ system that performs both measurement and power calculation online, without the need of a pc for post-processing analysis, as instead is done in the present bolometry electronics.

The limiting factor is the noise level of a tokamak's environment, which makes it difficult to achieve high signal quality even if the electronics are very performing. Nevertheless, the new system can be exploited during tokamak's operation and can work with many LIA configurations and low pass filter parameters.

The next steps after this work should focus on the implementation of the new electronics on a larger scale, with multiple bolometer heads and channels. A better noise characterization can be performed and potentially optimized filters and FPGA firmwares can be tested.

Bibliography

- [1] *AD7730/7730L Data Sheet*. https://www.analog.com/media/en/technical-documentation/data-sheets/ad7730_7730l.pdf.
- [2] I. Zammuto et al. “The new ASDEX upgrade upper divertor for special alternative configurations: Design and FEM calculations”. In: *Fusion Engineering and Design* 171 (2021). DOI: <https://doi.org/10.1016/j.fusengdes.2021.112468>. URL: <https://www.sciencedirect.com/science/article/pii/S0920379621002441>.
- [3] M Bernert et al. “Application of AXUV diode detectors at ASDEX Upgrade”. In: *The Review of scientific instruments* (2014). DOI: 10.1063/1.4867662.
- [4] M. Bernert et al. “The X-Point radiating regime at ASDEX Upgrade and TCV”. In: *Nuclear Materials and Energy* (2023). DOI: 10.1016/j.nme.2023.101376.
- [5] Matthias Bernert. “Bolometry with diodes at the tokamak ASDEX Upgrade”. Master’s thesis. Technische Universität München, 2010.
- [6] Jeffrey Friedberg. *Plasma Physics and Fusion Energy*. Cambridge, 2007.
- [7] L Giannone et al. “Prototype of a radiation hard resistive bolometer for ITER”. In: *Plasma Physics and Controlled Fusion* (2005). DOI: 10.1088/0741-3335/47/12/004. URL: <https://dx.doi.org/10.1088/0741-3335/47/12/004>.
- [8] L. Giannone, K. Mast, and M. Schubert. “Derivation of bolometer equations relevant to operation in fusion experiments”. In: *Review of Scientific Instruments* (2002). DOI: 10.1063/1.1498906. URL: <https://doi.org/10.1063/1.1498906>.
- [9] D.N. Hill. “A review of ELMs in divertor tokamaks”. In: *Journal of Nuclear Materials* (1997). DOI: [https://doi.org/10.1016/S0022-3115\(97\)80039-6](https://doi.org/10.1016/S0022-3115(97)80039-6). URL: <https://www.sciencedirect.com/science/article/pii/S0022311597800396>.
- [10] Akos Horvath and Elisabeth Rachlew. “Nuclear power in the 21st century: Challenges and possibilities”. In: *Ambio* (2016). URL: <https://doi.org/10.1007/s13280-015-0732-y>.
- [11] *Lock in Amplifier on LabVIEW FPGA - NI Community*. <https://forums.ni.com/t5/Example-Code/Lock-in-Amplifier-on-LabVIEW-FPGA/ta-p/3500412>.

- [12] K. F. Mast et al. “A low noise highly integrated bolometer array for absolute measurement of VUV and soft x radiation”. In: *Review of Scientific Instruments* (1991). DOI: 10.1063/1.1142078. URL: <https://doi.org/10.1063/1.1142078>.
- [13] Susanne Pfalzner. *An Introduction to Inertial Confinement Fusion*. CRC Press, 2006.
- [14] Felix Reimold et al. “Divertor studies in nitrogen induced completely detached H-modes in full tungsten ASDEX Upgrade”. In: *Nuclear Fusion* 55 (2015).
- [15] Eugenio Schuster. *Nuclear Fusion and Radiation, Lecture 7*. 2015.
- [16] Steven W. Smith. *The Scientist and Engineer’s Guide to Digital Signal Processing*. California Technical Publishing, 1999.
- [17] ASDEX Team. “The H-Mode of ASDEX”. In: *Nuclear Fusion* 29.11 (1989). DOI: 10.1088/0029-5515/29/11/010. URL: <https://dx.doi.org/10.1088/0029-5515/29/11/010>.

Acknowledgement

The last year was incredibly beautiful and so dense of experiences. After concluding it I have to thank so many people I don't even know where to start from. First of all, I would like to thank my supervisor Prof. Alessandro Gabrielli and Dr. Fabrizio Alfonsi, who passionately taught me everything about FPGA programming: a beautiful and mysterious world well suited for a nerd and electronics enthusiast like I am.

A huge thank you to the University of Bologna. During last year I decided to take some courses from the Energy Engineering department because I am convinced that Physics, alone, is not enough for what I want to do. So I could explore the worlds of nuclear energy, fission and fusion, thanks to prof. Manservigi, Dr. Stanzani and prof. Sumini, who let us engage in complex projects where we had to design and simulate plasma engines and nuclear reactors.

Thank you to the Physics department and to all my professors, like prof. Finelli, Spighi, Scioli, Baldazzi... who taught me so much about nuclear physics and its applications.

Of course thank you to my colleagues both from Physics and from Energy Engineering: studying, giving exams, hanging out, eating indian food, gricia, tigelle and crescentine, developing projects with you and seeing that they worked was just beautiful.

An incredibly huge thank you goes to my family, my aunt and my parents. Needless to say, without my parents I could not have done any single thing that you've read in this thesis. Thanks for always supporting me and letting me believe in my dreams.

Thank you to my lifelong friends, who will always be in my life, even without knowing it. Thank you Ile for always being there. Thank you Giovi and Eriku.

And finally, well... what can I say? From the bottom of my heart, an immense thank you to all IPP!!! It's difficult to describe how thankful I am to you. I was dreaming of working in nuclear fusion for the last 7 years at least. I didn't think I could ever come to this point, but now I am finally part of this wonderful family. Thank you to all the friends and people I had the pleasure to cross my life with. We did so many things together: cooking cakes, chilling on sofas, carving pumpkins, walking on iced lakes, playing games and beer pong with water (I don't drink alcohol... crazy for being in Germany, I know), coffee breaks, trips and hikes, the master student poster event... Each of you gave me something that will be with me forever. You made my stay at IPP, which was already a dream, even better than every expectation I could have.

Of course a special thank you goes to my supervisor Matthias, for teaching me so many things, even in late evenings, and for your continuous support with the electronics and everything else. Combining fusion and electronics was the coolest project I have ever done in my life.

Special thanks to the electronics department of IPP, in particular Andi, Ludwig and Horst, who designed the new bolometer electronics and were always available when I

had questions.

When I first arrived at IPP it was like a sort of dream, I was working on what I used to learn at university and read on textbooks... but as the months passed it became better and better. Entering the vacuum vessel of AUG, the control room, participating in the last AUG campaign and, most importantly, seeing how everyone works hard to make everything go smooth. Everyone putting effort to understand the misteries of that huge and complex machine that is ASDEX Upgrade. When I think about nuclear fusion this is what comes to my mind. Imagining that we can in principle harvest energy from this is unbelievable. From its discovery, nuclear fusion has always been *30 years in the future* because of its tremendous number of challenges. But now more than ever all the World is putting so much effort that we will surely see something in the next 30 years.

No matter how hard it is... We will bring Nuclear Fusion to humanity.